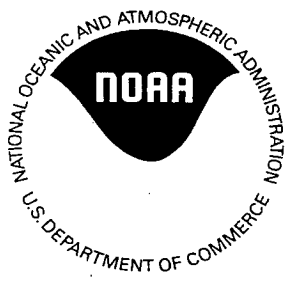

NOAA TECHNICAL MEMORANDUM
NWS WR-254

CONDITIONAL SYMMETRIC INSTABILITY --- METHODS OF OPERATIONAL DIAGNOSIS AND CASE STUDY OF 23-24 FEBRUARY 1994 EASTERN WASHINGTON/OREGON SNOWSTORM

Gregory A. DeVoir
National Weather Service Forecast Office
Boise, ID

May 1998

UNITED STATES
DEPARTMENT OF COMMERCE
William M. Daley, Secretary

National Oceanic and
Atmospheric Administration
D. James Baker, Under
Secretary and Administrator

National Weather Service
John J. Kelly, Jr., Assistant
Administrator for Weather Services

This publication has been reviewed
and is approved for publication by
Scientific Services Division,
Western Region

Delain A. Edman, Chief
Scientific Services Division
Salt Lake City, Utah

TABLE OF CONTENTS

LIST OF FIGURES

Conditional Symmetric Instability
Methods of Operational Diagnosis and Case Study
of 23-24 February 1994 Eastern Washington/Oregon Snowstorm

Gregory A. DeVoir
National Weather Service Forecast Office
Boise, Idaho

I. Introduction

Atmospheric stability is one of the most important parameters for meteorologists to assess on a daily basis. Errors in the diagnoses of various types of atmospheric stability can lead to large discrepancies between expected and observed weather conditions and adversely affect the activities of public, private and commercial interests. To mitigate such negative effects, forecasters must strive for an ever-increasing knowledge of the different types of atmospheric instabilities they may encounter on a daily basis.

Conditional Symmetric Instability (CSI), commonly referred to as "slantwise convection," is one such instability. Work by Bennetts (1975), Bennetts and Hoskins (1979) and Emanuel (1980, 1983a,b) firmly established CSI theory. More recently, Snook (1992), Moore and Blakley (1988), Moore and Lambert (1993), and others have documented the various operational methods of CSI detection developed during the late 1970s and 1980s.

CSI has been linked to the development of narrow, mesoscale cloud and precipitation bands in areas stable to upright convection. Forecast errors due to the manifestation of CSI in the atmosphere can be quite large; Much greater-than-expected amounts of rain or snow often occur, along with drastic gradients in both the intensity and amount of precipitation across a small area.

While meso-β scale (~30-300 km) mechanisms such as slantwise convection are too small to be resolved at the grid scale of today's operational numerical models, most of the larger-scale dynamical mechanisms and thermodynamic processes leading to CSI precipitation banding are handled quite well.

The purpose of this Technical Memorandum is to help forecasters better understand CSI theory, enabling them to both recognize and anticipate its forecast implications. Section 2 presents a detailed review and discussion of dynamical CSI theory. Mathematical relationships describing the CSI synoptic environment and stability characteristics of symmetric flow are examined. In

Section 3, aspects of CSI assessment and various techniques useful in diagnosing CSI are reviewed and illustrated. Next, synoptic-scale mechanisms which help to maintain slantwise circulations over extended periods of time are discussed in Sections 4 and 5. Special attention is given to the presence of frontogenesis and enhanced ageostrophic circulations within regions of CSI.

Finally, a detailed case study in which CSI contributed to a record-breaking precipitation event in the Pacific Northwest is presented in Section 6. Methods of CSI detection from Section 3 are used to evaluate the presence of CSI during the event, and synoptic forcing mechanisms which appeared to maintain the duration and intensity of CSI circulations over the region are identified.

II. Symmetric Instability Theory

a. Description

Symmetric instability (SI) theory is based upon the concept of 'symmetric flow' and the method of assessing the stability of that flow. According to Bluestein (1993), a symmetric flow is "one whose basic state and perturbations are independent of some horizontal coordinate, which is here designated as the x direction". This condition can be represented graphically by a parcel taking the form of an infinitely long tube extending in both directions along the x axis (Fig. 1). Hence, the tube in this figure is expected to have the same properties all along the x-axis - a symmetric flow.

In the early 1980s, Emanuel (1983b) developed a parcel-analysis technique for symmetric flow (from which Fig. 1 was conceived). Analogous to standard convective parcel theory, a parcel (in this case, the tube) is displaced along a *slanted* plane (rather than vertically) and the restoring force is examined. If the parcel becomes positively buoyant in the direction of slantwise displacement, SI exists.

SI combines the effects of static (gravitational) and inertial (horizontal) stabilities that result from the distribution of forces acting on an air parcel. Studies by Emanuel (1979) and Bennetts and Hoskins (1979) showed that the atmosphere can be stable to horizontal and vertical displacements, yet *unstable* to *slantwise* displacements. SI represents the slantwise acceleration resulting from a combination of these forces.

b. Static and Inertial Stability

As is well known, static stability describes the atmosphere's resistence to vertical displacements. Vertical buoyancy of an air parcel results in the vertical mixing of heat and moisture. Inertial stability describes the atmosphere's resistence to horizontal displacements. Imbalances in the horizontal wind field can result in the lateral mixing of momentum. To achieve SI, the atmosphere must be both statically stable ($\partial\theta/\partial z>0$) and inertially stable (absolute geostrophic vorticity ($f+\zeta_g$)>0).

Since much about the synoptic-symmetric environment can be described in terms of inertial stability, a brief discussion is presented here. Holton (1985) showed that inertial instability exists when the absolute vorticity of the basic flow is less than zero. Since absolute vorticity is

nearly always positive on the synoptic scale, forecasters can usually assume the atmosphere is inertially stable. On occasion, however, the above condition is satisfied on the anticyclonic side of a strong wind speed maximum.

Inertial instability is defined by the following mathematical expression (Holton 1985):

$$(f+\zeta_g) < 0 \quad (2.1),$$

Absolute Geostrophic Vorticity < zero,

where f is the Coriolis parameter, ζ_g is the relative geostrophic (vertical) vorticity, and $(f+\zeta_g)$ is the absolute geostrophic vorticity of the flow. **(2.1)** can be expanded by expressing (ζ_g) in terms of the geostrophic wind components, u_g and v_g, to yield:

$$(f+\zeta_g) = f + \left(\frac{\partial v_g}{\partial x} - \frac{\partial u_g}{\partial y}\right) < 0 \quad (2.2).$$

Let us now consider a base-state geostrophic flow (no variation of wind speed in the x direction) in the Northern Hemisphere with a wind speed maximum embedded within that flow (Fig. 2). Since $\partial v_g / \partial x = 0$ in the defined base-state flow, the expression for inertial instability becomes:

$$f - \left(\frac{\partial u_g}{\partial y}\right) < 0 \quad (2.3).$$

Therefore, given a sufficiently-strong jet-streak embedded within the base-state geostrophic flow, the relative geostrophic vorticity of the flow ($\partial u_g / \partial y$) in the vicinity of the speed maximum may potentially exceed the earth's vorticity (f), resulting in negative absolute geostrophic vorticity over that area. That is to say that the speed shear between points Y1 and Y2 must become greater than f.

The presence of negative absolute vorticity would trigger the immediate release of inertial instability, allowing air to mix horizontally and reduce the shear until the absolute geostrophic vorticity was again positive. Inertial-gravity waves can result from such a response, potentially lifting air to its lifting condensation level and forming precipitation (Bluestein 1993). The atmosphere must be inertially stable to rule out the possibility of precipitation bands induced by inertial-gravity waves. However, small *positive* inertial stability (strong vertical wind shear and low absolute vorticity through a deep layer) create a favorable environment for SI, as will be shown in the following section.

c. Conditional Symmetric Instability

Up to now, this discussion has focused on properties of symmetric flow and SI. In assessing CSI, we seek to understand the forecast implications of moisture (sufficient to produce clouds and precipitation) within a symmetrically unstable environment. While SI can occur in a dry environment, a near-saturated environment is necessary for slantwise-convective precipitation bands to develop; Saturation is the "conditional" descriptor in CSI.

CSI is usually a cool season phenomenon and typically occurs within larger regions of upward vertical motion (hence, saturation) and precipitation. As such, it is most often diagnosed in the vicinity of warm fronts. CSI manifests itself in the atmosphere as two-dimensional, sloped rolls aligned with the geostrophic shear (thermal wind).

Figure 3 (from Colman 1992) is a cross-section showing the perturbation stream function which results from CSI. The thermal wind is perpendicular to the cross-section (coming out of the page). The rolls slope toward the cold air and are on average 50-100 km wide and 100-400 km long (Moore 1996). The rolls have spacing on the order of 50 to 100 km or less, depending on the slope of the isentropes and depth of the unstable layer (Jascourt et al. 1988).

As previously mentioned, the atmosphere must be statically stable ($\partial\theta/\partial z>0$ in a non-saturated environment) for SI to be the preferred mode of atmospheric response. For CSI to occur, the atmosphere must be nearly-saturated. Therefore, since equivalent potential temperature (θ_e) is conserved for moist processes such as CSI, the condition for CSI becomes $\partial\theta_e/\partial z>0$ (small but positive *moist* static stability) in a near-saturated environment.

Positive static stability is required due to the differing growth rates of convection resulting from CSI and convective instability. Slantwise convection associated with CSI occurs on the time scale of mesoscale processes and can therefore take several (~3-4) hours to develop into mature precipitation bands. On the other hand, upright convection can develop in tens of minutes. Therefore, given the co-existence of CSI and convective instability in a given layer of the atmosphere, upright convection will dominate slantwise convection.

The relationship between SI, static/inertial stabilities and the synoptic environment can be better understood by examining the following relationship. Bluestein (1993) derived the following expression as a necessary condition for SI:

$$f^2\left(\frac{(\zeta_g+f)}{f}-\frac{1}{Ri}\right) < 0 \qquad (2.4),$$

where (ζ_g+f) is the absolute geostrophic vorticity, and Ri is the Richardson number (static stability divided by the vertical wind shear). Ri is given by the following expression:

$$Ri = \frac{\frac{g}{\theta}\frac{\partial\theta}{\partial z}}{\left(\frac{\partial u_g}{\partial z}\right)^2} \qquad (2.5),$$

where $\partial\theta/\partial z$ is the static stability and $(\partial u_g/\partial z)^2$ is the vertical geostrophic wind shear. Bluestein showed that SI exists within a non-saturated layer when **(2.4)** yields a negative result.

To assess CSI within a near-saturated environment, it is necessary to substitute a moist Richardson number (Ri_{moist}) for Ri into **(2.4)** (Bluestein, personal communication). Following Emanuel

(1983a), Ri_{moist} can be calculated using:

$$Ri_{moist} = \frac{\frac{g}{\theta_e}\frac{\Gamma_m}{\Gamma_d}\frac{\partial \theta_e}{\partial z}}{\left(\frac{\partial u_g}{\partial z}\right)^2} \quad (2.6),$$

where Γ_m/Γ_d are the moist/dry adiabatic lapse rates, respectively, and $\partial\theta_e/\partial z$ is the moist static stability. Combining **(2.4)** and **(2.6)** yields the following conditional expression for CSI:

$$\frac{\frac{g}{\theta_e}\frac{\Gamma_m}{\Gamma_d}\frac{\partial \theta_e}{\partial z}}{\left(\frac{\partial u_g}{\partial z}\right)^2} < \left(\frac{f}{(\zeta_g + f)}\right) \quad (2.7),$$

$$\therefore \frac{\frac{g}{\theta_e}\frac{\Gamma_m}{\Gamma_d}\frac{\partial \theta_e}{\partial z}}{\left(\frac{\partial u_g}{\partial z}\right)^2} \bullet \frac{(\zeta_g + f)}{f} < 1 \quad (2.8).$$

Several synoptic and dynamic characteristics of the ambient CSI environment can be understood using **(2.8)**. As the absolute geostrophic vorticity ($\zeta_g + f$) and moist static stability ($\partial\theta_e/\partial z$) become small, or as the vertical wind shear $(\partial u_g/\partial z)^2$ increases (indicating small inertial stability/slight anticyclonic shear), CSI becomes more likely. As discussed in the previous section, strong vertical wind shear promotes small but positive inertial stability, a necessary condition for symmetric instability.

Therefore, it is clear that synoptic environments characterized by small, but positive static/inertial stability and strong vertical wind shear are favorable for the development of CSI circulations, given sufficient lift and moisture to reach saturation. Such conditions are often met in the vicinity of warm fronts where small positive inertial stability is indicated by small values of absolute vorticity through a deep layer (slight anticyclonic shear) and strong vertical wind shear.

Remember that a conditional-symmetrically unstable atmosphere will attempt to gain neutrality within a several-hour period. The presence of neutral or small positive symmetric stability occurring within a well-mixed, nearly-moist adiabatic layer strongly suggests the presence or recent occurrence of slantwise convective adjustment. The next section will discuss the qualitative indicators which aid the forecaster in assessing CSI.

III. CSI Assessment

a. Qualitative Indicators

Qualitative indicators of CSI include (1) strong vertical wind shear, (2) a well-mixed layer close to saturation, and (3) multiple cloud bands aligned parallel to the thermal wind (1000-500 mb thickness field). The presence of these conditions in concert with small static and inertial stability should be cause for further CSI investigation. While cloud bands cannot be observed ahead of time, today's operational numerical models can be used to assess the synoptic environment's susceptibility to CSI well in advance of an event.

Qualitative investigations of CSI usually involve the examination of cross-sections

of geostrophic angular momentum (M_g, see **(3.1)**) and equivalent potential temperature (theta-E or θ_e) constructed normal to the mid-tropospheric temperature gradient/thermal wind (Fig. 4); For convenience, forecasters may use the 1000-500 mb thickness field. The cross-sections must be aligned normal to the thickness field so that the wind shear is mostly speed shear (versus directional shear) and is normal to the cross-section (Moore, personal communication). Emanuel (1983b) demonstrated the utility of this technique to diagnose symmetric instability from synoptic data.

Figure 5, adapted from Sanders and Bosart (1985), is a schematic vertical cross-section illustrating CSI. Dashed lines represent constant θ_e surfaces, while solid lines represent constant M_g surfaces. **The atmosphere is assumed to be saturated throughout the cross-section. CSI exists in areas where the slope of M_g surfaces (lines of constant geostrophic angular momentum) is less (flatter) than those of θ_e surfaces.** Studying the resultant motions of air parcels undergoing vertical, horizontal, and slantwise displacements shows why this is true.

The resultant forces of parcels undergoing displacements in Fig. 5 can be narrowed down to 1) vertical acceleration (up or down), and 2) horizontal acceleration to the left or right of M_g surfaces in the cross-section. Horizontal accelerations are due to decreasing/increasing M_g of the parcel's post-displacement environment (the parcel either needs to speed up or slow down to match the M_g of its new environment).

Looking at Fig. 5, purely horizontal displacements (as with parcel A) result in positive buoyancy (since θ_e of the parcel is greater than θ_e of the environment) and horizontal deceleration (since M_g of the environment is less than M_g of the parcel). The parcel eventually becomes colder than its environment as it rises, causing A to descend and warm before returning to equilibrium (θ_e of the parcel becomes equal to θ_e of the environment).

For purely vertical displacements (as with parcel C), the result is negative buoyancy (since θ_e of the parcel is less than θ_e of the environment) and horizontal acceleration (since M_g increases with height). During descent, θ_e of the parcel increases (warms) and M_g decreases (slows) to match the θ_e and M_g of the environment; The parcel returns to C.

However, through a combination of displacements in the vertical and horizontal (as with parcel B), we see that an acceleration in the direction of displacement results from a slantwise displacement (positive buoyancy and horizontal acceleration). In the slantwise direction of displacement, θ_e of the parcel is greater than θ_e of the environment and M_g of the parcel is less than M_g of the slantwise environment. Slantwise displacement leads to positive buoyancy and acceleration in the direction of the slantwise displacement. Continued displacement in the slantwise direction will lead to the formation of slantwise-convective precipitation bands to restore the atmosphere to neutral or positive conditional symmetric stability.

With few exceptions, isentropic and likely θ_e surfaces will be close to vertical in regions of low but positive static stability

(Moore and Lambert 1993). In addition, the slope of M_g surfaces is inversely proportional to the vertical wind shear (the greater the vertical wind shear, the flatter M_g surfaces become). This can be seen from the following relationship,

$$M_g = V_g + fx \quad (3.1),$$

where $\mathbf{V_g}$ is the geostrophic wind, $\boldsymbol{f}$ is the Coriolis parameter, and $\mathbf{x}$ is the distance from the left side of a vertical cross-section. Since M_g increases proportionally with V_g, M_g surfaces become more horizontal as wind speeds increase with height in the cross-section. It is once again apparent that low positive static stability and strong vertical wind shear increase the potential for CSI.

An example of this technique using actual synoptic data is shown in Fig. 6 (from Moore and Lambert 1993). The dashed-line contours identify regions of CSI within the cross-section. Note that our investigation focuses on identifying symmetrically unstable layers within the cross-section. Further assessment of the moisture content within that layer will determine if and where CSI may occur.

For further information concerning the use of M_g for CSI assessment, please see the Appendix ("Why Momentum Surfaces?")

b. Quantitative Methods

I. SCAPE

Quantitative methods have also been formulated to assess CSI. As mentioned earlier, Emanuel (1983b) developed a general parcel method by which Slantwise Convective Available Potential Energy (SCAPE) can be calculated from standard synoptic data.

Atmospheric soundings can be constructed along M_g surfaces and values of SCAPE computed. The calculation of SCAPE is analogous to the computation of Convective Available Potential Energy (CAPE) used to assess upright convective potential, only an inertial term is included in the SCAPE computation.

Values of SCAPE in CSI case studies generally range from 50 to 300 J kg^{-1}. These values of SCAPE are small compared to typical values of CAPE, but are nonetheless are large enough to create a symmetrically unstable environment in a statically stable atmosphere. And in some cases, these relatively small SCAPE values may be sufficient to release existing conditional gravitational instability within a layer, initiating upright convection.

Jascourt et al. (1987) studied the puzzling orientation of narrow bands of deep, upright convection over Louisiana and eastern Texas on a day when free convection was expected. The bands of upright convection were aligned parallel with the thermal wind. The organization of the upright convection, combined with the observance of numerous qualitative CSI indicators, suggested that a combination of convective and conditional symmetric instability organized the upright convection into mesoscale bands aligned with the 1000-500 mb thickness gradient. This conclusion supported previous work by Emanuel (1980).

CSI assessments using SCAPE are difficult to make due to the lack of temporal and spatial resolution inherent in upper-air soundings. Fortunately, another quantitative parameter may be used to assess CSI.

II. Equivalent Potential Vorticity (EPV)

The use of **E**quivalent (moist) **P**otential **V**orticity (EPV) makes quantitative assessment of CSI much easier and more complete than the SCAPE procedure described above. It can be shown that CSI exists in those areas where EPV < zero (Bennetts and Hoskins 1979, Moore and Lambert 1993). Given negative EPV, low static stability, upward vertical motion and sufficient moisture, slantwise convection will ensue. The slantwise accelerations resulting from moist symmetric instability are atmospheric responses to restore EPV to its neutral (zero) value (Shapiro 1982).

The requirement that EPV be negative in a convectively stable atmosphere is equivalent to the criterion that slopes of M_g surfaces be shallower than slopes of θ_e surfaces. Therefore, areas of negative EPV should mirror analyzed CSI layers from vertical cross-sections of M_g and θ_e (Figs. 6 and 7). Given sufficient model and data set resolution, this should always occur. However, since CSI is a true mesoscale instability, current operational numerical models' spatial and temporal resolutions become very important when considering EPV calculations.

Generally speaking, a model must have 40 km resolution or better to define CSI regions (Moore, personal communication). The Nested Grid Model (NGM) and early ETA model can often resolve conditional symmetric neutrality (CSN), where M_g and θ_e surfaces nearly align. Therefore, PCGRIDDS, NTRANS or GARP can be used to assess regions of CSN, and in some cases resolve true CSI. As one might suspect, best results have been attained during studies using mesoscale models with higher resolution gridded datasets.

IV. Operational Diagnosis of CSI

Several real-time data sources can be utilized in concert with numerical model fields to observe qualitative indicators of CSI, including radar, satellite imagery and wind profilers. Examining geopotential height and wind fields in both plan and cross-section modes can reveal areas of small static stability, strong vertical wind shear and weak anticyclonic shear. The forecaster can then examine static stability in conjunction with appropriate diagnostics by constructing vertical cross-sections of M_g and θ_e, EPV and relative humidity.

Since the manifestation of CSI requires a nearly-moist adiabatic layer, special emphasis should be placed upon locating and tracking potential lifting mechanisms such as surface convergence zones, fronts and upper-level jet streaks. The sustained upward vertical motion generated by these features may be sufficient to saturate a conditional-symmetrically unstable layer, releasing the slantwise instability and enabling slantwise-convective adjustment to occur.

V. CSI and Frontogenesis

As is well known, frontogenesis results in an ageostrophic circulation as the

atmosphere strives to attain equilibrium. Geostrophic confluence acts frontogenetically, or to increase the horizontal temperature gradient. This process disrupts the thermal wind balance (Hoskins and Bretherton 1972) and an ageostrophic, thermally-direct circulation (DTC) forms to restore balance.

Figure 8 (from Uccellini and Kocin 1987) is a schematic of divergence and ageostrophic wind circulations in the entrance and exit regions of a straight jet streak. Figure 8A is the classic "4-quadrant" conceptual model of an upper-level jet streak, depicting areas of divergence and convergence in each quadrant. Figure 8B illustrates the resulting ageostrophic thermal circulations (both direct and indirect) induced in the entrance and exit regions of the jet, respectively.

Sanders and Bosart (1985) examined the mechanisms responsible for intense mesoscale snow bands observed in the snowstorm of 11-12 February 1983. They discovered a greatly enhanced frontal circulation in the presence of small moist symmetric stability. Figure 9 (Emanuel 1985) shows the ageostrophic mass stream-function in a cross-section taken through the bands. Note the presence of a concentrated sloping updraft (denoted by the solid-dashed line) approximately 100 km away from the axis of maximum frontogenetical forcing (heavy dashed line).

Emanuel (1985), Sanders and Bosart (1985) and Moore and Blakley (1988) showed that when frontogenesis occurs within CSI environments (weak or negative symmetric stability), significant intensification of frontal circulations can develop (Fig. 10). The frontogenetic DTC, which has a sloping trajectory up the warm side of the frontal boundary, reduces in horizontal scale and intensifies.

Figure 10A shows a typical frontal circulation, while figure 10B shows the horizontal contraction and vertical intensification of the frontal circulation in the presence of neutral or small symmetric stability (EPV=0 or small positive values of EPV). While the symmetrically unstable circulation brings the atmosphere back to a state of neutrality or very small stability, frontogenesis within the neutral or small symmetrically-stable environment intensifies the original slantwise circulation, allowing the slantwise-convective precipitation bands to persist and even intensify long after the SCAPE has been used up (Bluestein 1993).

Forecasters are strongly urged to examine frontogenesis and jet streak circulations in areas where CSI may be present. The next section examines a case study in which these- mechanisms appear to have been responsible for unexpected heavy snow in portions of the Pacific Northwest on 23-24 February 1994.

VI. Case Study

a. Introduction

The preceding sections on CSI theory and operational detection will now be used to investigate the role CSI may have played during an unexpected heavy snow event over the interior Pacific Northwest

on 23-24 February 1994. For this study, gridded-data files from the NGM and Eta models were viewed from 1200 UTC 23 February 1994 to 1200 UTC 24 February 1994; Surface and upper-air data were examined using GEMPAK. GOES-7 satellite imagery (visible, IR, and water vapor) was also examined. Radar coverage at the time of this event was unavailable over south-central Washington and northern Oregon (KPDT WSR-88D became available in 1995).

Localized heavy snowfall occurred over southern Washington state and northern Oregon beginning late in the evening of February 23rd and lasting through much of the 24th. Drastic gradients in snowfall accumulation (Figs. 11-12) and intensity were observed during the event in southern Washington and northern Oregon. Remarkable snowfall rates were observed within narrow snowbands aligned from west to east, at times exceeding 3-4 inches per hour.

While locally heavy coastal rain and mountain snow was expected west of the Cascade crest, a strong west-northwest flow was expected to result in drying-downslope winds throughout the Yakima Valley and Columbia River Basin. However, by 1800 UTC 24 February 1994, bands of heavy snow had dropped from 6 to 16 inches of snow from the lower east slopes of the Washington Cascade foothills to the Blue Mountains of northeast Oregon. Pendleton WSO recorded 16.1 inches, establishing a new 24-hour snowfall record. Yakima WSO received 8.2 inches from the storm, its single largest snowfall of the winter of 1993-1994.

Much heavier-than-expected precipitation occurred west of the Cascade crest as well; Crystal Mountain Ski Area in the central Washington Cascades established a new 24-hour snowfall record with 65 inches, and Portland, Oregon recorded its third-greatest 24-hour rain total (2.46 inches) on record. Storm spotters from communities surrounding Portland reported 24-hourly rain totals of nearly 5 inches.

b. Synoptic Overview

The usual method for forecasting snow in areas of Washington and Oregon east of the Cascade crest is to estimate orographic effects in conjunction with quasi-geostrophic forcing and available moisture. Usually, a significant southerly component to the lower-level wind field must be present for warm advection precipitation to reach climatological precipitation shadows east of the Cascades in Washington and Oregon These downslope areas are clearly visible in climatological precipitation maps (Figs. 13 and 14) for Washington and Oregon.

Throughout the 23-24 February 1994 event, model guidance indicated strong west-northwest flow in the middle and upper troposphere. Little if any precipitation was expected in typical rain-shadowed areas east of the Cascades.

The 0000 UTC 24 February 1994 500 mb NGM initialization (Fig. 15) shows an energetic shortwave located along the southwestern British Columbia coast. The shortwave was rotating around a deep 522 dm low centered over south central British Columbia at 500 mb. The corresponding mid- to upper-level height gradient was tight in association with the

digging shortwave, inducing moderate to strong west-northwest winds in the middle and upper troposphere over Washington and Oregon.

Figure 16 shows the 2300 UTC 23 February 1994 visible GOES-7 image of the northwest U.S. A large area of clearing associated with downslope flow is evident east of the Cascades in both central Oregon and in central/eastern Washington.

The 0000 UTC Feb 24 NGM surface pressure and 1000-500 mb thickness analysis (Fig. 17) shows a surface low over central Montana with strong cold air advection over Washington. The atmosphere was well-mixed on this afternoon as maximum temperatures reached the 40s and 50s throughout most of eastern Washington. However, by late afternoon, surface dewpoints had dropped into the teens in northeast Washington, indicative of an arctic boundary seeping southward out of British Columbia.

The shallow arctic cold front progressed steadily southward through eastern Washington during the late afternoon and evening hours of February 23. Computations of Pettersson's frontogenesis function (Fig. 18) viewed using PCGRIDDS indicate that this boundary was frontogenetical.

By 0300 UTC Feb 24, light snow began to fall in many parts of central and south-central Washington. Occasional light snow continued throughout the late evening, leaving up to an inch of accumulation in central Washington. The snow accompanied the passage of the shallow arctic front/dewpoint boundary. The boundary sagged farther southward until around midnight PST, when it became stationary in northern Oregon.

Satellite imagery showed the development of mesoscale cloud bands aligned from west to east over the Washington Cascades from 0030 to 0630 UTC 24 February 1994 (Figs. 19a-d). This corresponded well with the onshore movement of a strong 300 mb jet streak (130 knots) between 0000 and 1200 UTC, as shown in Figs. 20 and 21.

As the 300 mb jet streak moved onshore, moisture rapidly increased in northwest Oregon and southwest Washington (Figures 19c-g). It is believed that upper-level divergence/surface moisture convergence in the right-rear quadrant of the jet and a subsequent ageostrophic DTC saturated the lower troposphere in southern Washington and northern Oregon. Moisture convergence was supplemented by low-level lift from the frontogenetic arctic boundary along the Washington/ Oregon border.

This can be shown by looking at the respective contributions of moisture advection by the total wind and ageostrophic wind shown in Figs. 22 and 23. Figure 22 shows the mixing ratio advection by the total wind, while Fig. 23 shows mixing ratio advection by the ageostrophic wind. Note that moisture advection by the total wind is occurring primarily at 500-600 mb, with neutral/negative moisture advection occurring from below 800 mb at 44.5 degrees north, to below 600 mb at 47 degrees north.

Figure 23 clearly shows moisture advection by the ageostrophic wind from

500 mb to the surface. Maximum moisture advection occurs at 700 mb and below. Figures 22-23 strongly suggest that the intensified ageostrophic circulation induced by frontogenesis and upper-level jet forcing are responsible for saturating the lower layers over northern Oregon and south-central Washington in prevailing west-northwest flow. Very little in the way of low-level moisture advection (below 700 mb) is attributed to the total wind at 1200 UTC 24 February 1994.

Snow bands of increasing intensity developed over southern Washington and northern Oregon between 0800 and 1200 UTC as saturation occurred below 700 mb. Snow fell heavily at times from Yakima, WA to Pendleton, OR from 1000 UTC to 1800 UTC 24 February 1994.

c. CSI Assessment

Qualitative CSI indicators (discussed in Section 2) were present during the period of heaviest snowfall. Mesoscale precipitation bands were aligned parallel to the thermal wind (as evidenced by a comparison of Figs. 17 and 19) in the presence of strong vertical and anticyclonic wind shear. A vertical cross-section (defined in Fig. 24 and shown in Fig. 26) of θ_e and M_g shows the atmosphere to be conditionally unstable with respect to slantwise displacements over a large portion of south-central Washington and northern Oregon at 0000 UTC 24 February 1994 (Fig. 26). Relative humidity greater than 80% is indicated by the dashed lines, while θ_e is denoted by the thin solid lines.

A vertical cross-section of EPV at the same time (defined in Fig. 24 and shown in Fig. 27) shows neutral to negative values of EPV over much of southern Washington and northern Oregon at 0000 UTC 24 February. However, Fig. 26 also indicates the presence of convective instability below 700 mb (θ_e decreasing with height) to the north of 46 degrees north latitude in the area of highest relative humidity (dashed lines). This indicates that any convective development would be of the upright fashion south of 46 degrees north latitude given sufficient lift and moisture. Note that convective clouds are seen in Fig. 16 over northeast Oregon within this area of convective instability, but strong downsloping and subsidence eroded the cloud mass east of the Cascades in central Oregon and Washington.

Figures 28 and 29 show vertical cross-sections (defined in Fig. 25) of M_g/θ_e and EPV at 1200 UTC 24 February 1994. Convective instability is confined to locations south of 45 degrees north latitude. CSI continues to cover a large portion of south central Washington and northern Oregon at this time.

An area of negative EPV (Fig. 29) is evident while neutral to small positive values of EPV extended from southeast Washington through northern Idaho. This is consistent with recent ideas presented by Moore et al. (personal communication) concerning the spectrum of mesoscale instabilities present in the cool season environment. Convective instability is often found to the south, with CSI to the north, and weak convective-symmetric stability (slightly positive EPV) to the north of the CSI.

Neutral to small positive values of EPV are suggestive of slantwise atmospheric adjustment. Emanuel (1985) and others

showed that this type of environment (characterized by neutral or slightly positive EPV in the warmer air) is conducive to intense, thermally direct circulations in the presence of frontogenetical forcing, as discussed in the previous section.

Dramatic gradients in snowfall intensity were observed at this time in the south-central Washington snowbands. Along the northern edge of these banded snow showers, the sharp EPV gradient represented an increasingly stable environment with regard to slantwise displacements; Clear skies with dewpoints in the teens were observed 5 miles north of the intense snowbands in south-central Washington at 1200 UTC.

Lastly, an examination of ageostrophic circulation(s) over the area at 1200 UTC 24 February (Fig. 30) indicates the existence of an intense sloping updraft, remarkably similar to that shown in Fig. 9. The vertical wind profile, upper jet location and potential temperature structure are shown in Fig. 31. The ageostrophic circulation is indicated by thin arrows while the estimated ageostrophic mass streamfunction has been drawn over the circulation field. Note the presence of a strong, sloped updraft located roughly 125 km south of the region of maximum frontogenetical forcing (indicated by the heavy dashed line).

The ageostrophic DTC in Fig. 30 is the result of dynamics in the entrance region of the upper-level jet. The presence of frontogenesis (Fig. 18) in the lower levels suggests that the strong sloping updraft in Fig. 30 may have been locally enhanced by the formation of a secondary frontogenetic DTC within the CSI environment.

These conclusions support previous findings in the literature that CSI in the presence of frontogenesis leads to an intensification and horizontal constriction of the sloping updraft associated with the frontal circulation. This mechanism may indeed be responsible for the maintenance of the original slantwise convective circulations and locally heavy mesoscale snow bands in south-central Washington and northern Oregon on that day.

VII. Summary and Discussion

The manifestation of CSI in the atmosphere can initiate the formation of intense mesoscale cloud and precipitation bands. CSI theory and methods of CSI detection originally presented by Bennetts and Hoskins, Emanuel, Snook, Moore, and others have been summarized to aid forecasters' ability to diagnose areas of CSI from numerical model output and conventional observation systems (radar and satellite imagery).

Ageostrophic circulations induced by frontogenesis and upper-level jet streaks can maintain and intensify existing CSI circulations. Frontogenesis in areas of CSI has been shown to horizontally constrict and significantly intensify upward vertical motions in the vicinity of fronts, leading to intense mesoscale banding of clouds and precipitation.

While technological improvements in today's modernized forecast offices have made CSI assessment more accessible to forecasters, several challenges face

operational and research meteorologists alike.

First, the regional frequency and severity of cloud and precipitation banding associated with CSI is unknown. Climatological studies relating the frequency of precipitation banding occurrences to the depth and height (above ground level) of CSI layers and moisture parameters are needed to determine the significance and frequency of CSI heavy precipitation banding events. Without such studies, forecasters will continue to have difficulty quantifying what effects a given CSI layer may have in a given situation.

Additionally challenging is how to effectively convey this added information to the public. Similar to upright convection, CSI precipitation banding can affect small portions of an office's County Warning Forecast Area (CWFA).

Lussky (1989) suggested that forecast wording be enhanced during potential CSI banding situations to include the possibility of "locally heavier" rain or snow amounts over the affected area. NOWCASTs could then be utilized to inform users of the development and progress of heavier rain or snow bands.

Despite these challenges, the techniques discussed here should enable the reader to conduct his/her own real-time CSI examinations and case studies of banded precipitation. Improved understanding of the smaller-scale processes which drive our atmosphere will lead to more detailed forecasts and enhanced service to our customers and the meteorological community as a whole.

Acknowledgments. I would like to thank Philip Schumacher (SOO, WSO FGF) for insightful discussions during the early stages of this work, as well as Keith Meier (SOO, WSO BYZ) for providing PCGRIDDS datasets and offering many helpful comments during revision. Special thanks go to David Hogan (Forecaster, NWSFO SLC) for detailed snowfall and surface observations in eastern Washington/Oregon and to John Jannuzzi (MIC, NWSFO BOI) for improving readability aspects of the paper. Lastly, sincere appreciation goes to David (Rusty) Billingsley (SOO, NWSFO BOI) and Dr. Jim Moore (St. Louis University) for superb technical direction through the revision process which significantly improved and greatly facilitated the completion of this paper.

VIII. References

Barnes, S.L., and B.R. Colman, 1994: Diagnosing an operational model using Q-vector and potential vorticity concepts. *Mon. Wea. Rev.*, **9**, 85-102.

Bennetts, D.A., and B.J. Hoskins, 1979: Conditional symmetric instability - a possible explanation for frontal rainbands. *Quart. J. Roy.Meteor. Soc.*, **105**, 945-962.

Bluestein,H.B.,1993;Synoptic-Dynamic Meteorology in Midlatitudes, Volume II. *Oxford University Press.*

Colman, B.R., 1992: An example of conditional symmetric instability. Western Region Tech. Att. No. 92-03.

Dunn, L.B., 1988: Vertical motion evaluation of a Colorado snowstorm from a synoptician's perspective. *Wea. Forecasting*, **3**, 261-272.

Emanuel, K.A., 1980: Inertial instability and mesoscale systems. Part I: Linear theory of inertial instability in rotating viscous fluids. *J. Atmos* Sci., **36**, 2425-2449.

------, 1983a: The lagrangian parcel dynamics of moist symmetric instability. *J. Atmos.Sci.*, **40**, 2368-2376.

------, 1983b: On assessing local conditional symmetric instability from atmospheric soundings. Mon. Wea. Rev., **111**, 2016-2033.

------, 1985: Frontal circulations in the presence of small moist symmetric stability. *J. Atmos. Sci.*, **42**, 1062-1071.

------, 1988: Observational evidence of slantwise convective adjustment. *Mon. Wea. Rev.*, **116**, 1805-1816.

Jascourt, S.D., S.S. Lindstorm., C.S. Seman., and D.D. Houghton., 1988: An observation of banded convective development in the presence of weak symmetric stability. *Mon. Wea. Rev.*, **116**, 175-191.

Hoskins, B.J., and F.P. Bretherton, 1972: Atmospheric frontogenesis models: Mathematical formulation and solution. *J. Atmos. Sci.*, **29**, 11-37.

Holton, J.R., 1985: An introduction to dynamic meteorology. *Academic Press.*
Lussky, G.R., 1989: Heavy rains and flooding in Montana: A case for operational use of symmetric instability diagnosis. *Wea. Forecasting*, **4**, 186-201.

Moore, J.T., and P.D. Blakley., 1988: The role of frontogenetical forcing and conditional symmetric instability in the midwest snowstorm of 30-31 January 1982. *Mon. Wea. Rev.*, **116**, 2155-2171.

------, and T.E. Lambert., 1993: The use of equivalent potential vorticity to diagnose regions of conditional symmetric instability. *Wea. Forecasting*, **8**, 301-308.

Sanders, F., and L.F. Bosart., 1985: Mesoscale structure in the megalopolitan snowstorm of 11-12 February 1983. Part I: Frontogenetical forcing and symmetric instability. *J. Atmos. Sci.*, **42**, 1050-1061.

Snook, J.S., 1992: Current techniques for real-time evaluation of conditional symmetric instability. *Wea. Forecasting*, **7,** 430-439.

Thorpe, A.J., and K.A. Emanuel., 1985: Frontogenesis in the presence of small stability to slantwise convection. *J. Atmos. Sci.*, **42**, 1809-1824.

Uccellini, L.W., and P.J. Kocin., 1987: The interaction of jet streak circulations during heavy snow events along the east coast of the United States. *Wea. Forecasting,* **2**, 289-308.

Wolfsberg, D.G., K.A. Emanuel., and R.E. Passarelli, 1986: Band formation in a New England winter storm. *Mon. Wea. Rev.*, **114**, 1552-1569.

APPENDIX

Why Momentum Surfaces???

The following discussion (Moore, personal communication) addresses the questions of how and why vertical cross-sections of M_g are used to identify areas of CSI.

Look (again) at how M_g is defined (**3.1**, above); $\boldsymbol{M_g = V_g + fx.}$ Since V_g is the component of the wind normal to the plane of the cross-section, M_g can be used in the u equation of motion **(a)** as follows:

$$\frac{du}{dt} = -\frac{1}{\rho}\left(\frac{\partial p}{\partial x}\right) + fv \qquad (a).$$

Next, since $-fV_g = -\frac{1}{\rho}\left(\frac{\partial p}{\partial x}\right)$, *we have:*

$$\frac{du}{dt} = -fV_g + fv \qquad (b),$$

$$\therefore \frac{du}{dt} = f\,(V - V_g) \qquad (c).$$

Since $\boldsymbol{V = (M_{parcel} - fx)}$ *and* $\boldsymbol{V_g = (M_g - fx)}$, one can write **(c)** as:

$$\frac{du}{dt} = f\,(M_{parcel} - M_g) \qquad (d),$$

where M_g is the geostrophic angular momentum of the flow, and M_{parcel} is the absolute momentum of the parcel being displaced from its original location to a different environment. If the parcel is sub-geostrophic, it will need to speed up. If the parcel moves into a region where the environmental winds are weaker, it will need to slow down.

M values of the parcel and the environment (geostrophic background state) can be used to see if the parcel will accelerate left or right on the cross-sectional diagram. It is exactly parallel to the evaluation of the vertical component of motion (ω) when one compares θ (if the air is unsaturated) or θ_e values (if the air is saturated) of the parcel to the environment's θ or θ_e to see if the air parcel will tend to accelerate up or down or be neutrally buoyant. M values are just a way to compare the parcel inertia to the environment's geostrophic wind speed to see if the parcel "fits in" with the environment.

The orientation of the cross-section is very important. It must be aligned normal to the thickness field so that the wind shear is mostly speed shear and is normal to the cross-section. The plane of the cross-section is the x axis, which is why the du/dt equation can be used, while the y axis is into the cross-section.

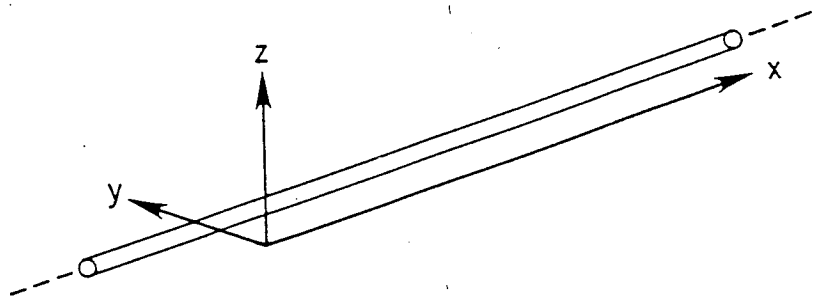

FIG. 1. A parcel takes the form of an infinitely long tube if there are no variations along the tube. In this illustration, the tube is aligned along the x-axis. In the "parcel" theory of symmetric instability, we displace this tube and see whether it is forced back to its original position or becomes positively buoyant in the direction of slantwise displacement. (From Bluestein 1993)

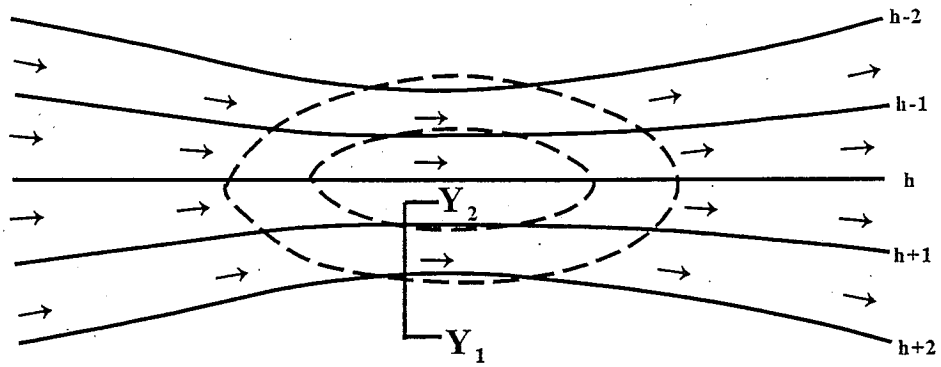

FIG. 2. Example of inertial instability in the vicinity of an upper-level wind speed maximum in base-state geostrophic flow. Dashed lines represent isotachs while solid lines represent height contours. Measuring the geostrophic wind velocities at Y2 and Y1, inertial instability exists if $(\partial u_g/\partial y) > f$, causing the absolute vorticity of the flow to become negative. Inertial instability would result in lateral mixing of momentum, reducing the shear until the absolute vorticity of the flow became positive.

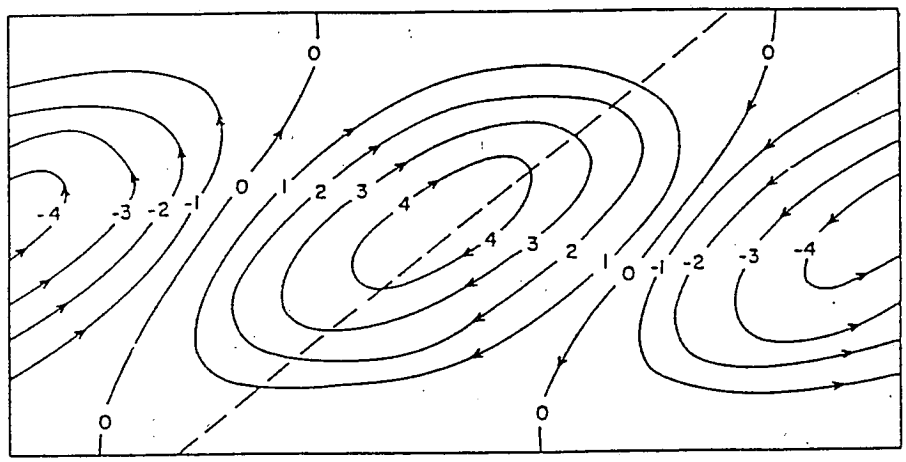

FIG. 3. Perturbation streamfunction resulting from CSI. The thermal wind is perpendicular to the figure and slantwise convective rolls slope towards the cold air in the positive Y direction. (from Colman 1992).

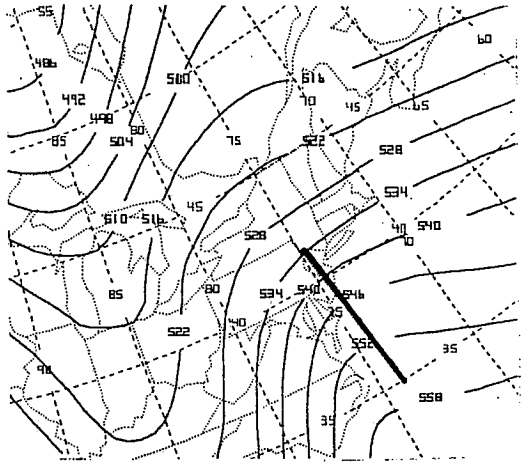

FIG. 4. Investigations of the presence of symmetric instability are accomplished by constructing vertical cross-sections oriented normal to the thermal wind shear vector. In this case, cross-sectional coordinates are oriented perpendicular to the 1000-500 mb thickness field.

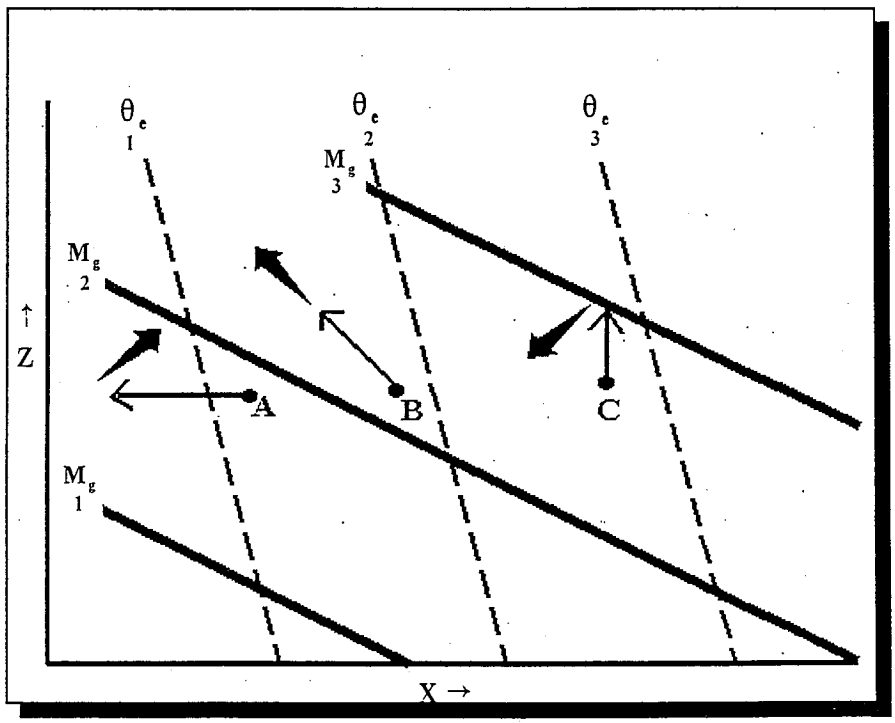

FIG. 5. Vertical cross-section illustrating symmetric instability. Dashed lines represent equivalent potential temperature (θ_e) and solid lines denote absolute geostrophic momentum (M_g) of the flow ($\theta_{e1}<\theta_{e2}<\theta_{e3}$ and $M_{g1}<M_{g2}<M_{g3}$). Light arrows represent the direction of displacement of parcels A, B and C, while solid arrows denote resultant parcel motions from respective horizontal, vertical and slantwise displacements. (Adapted from Sanders and Bosart, 1985).

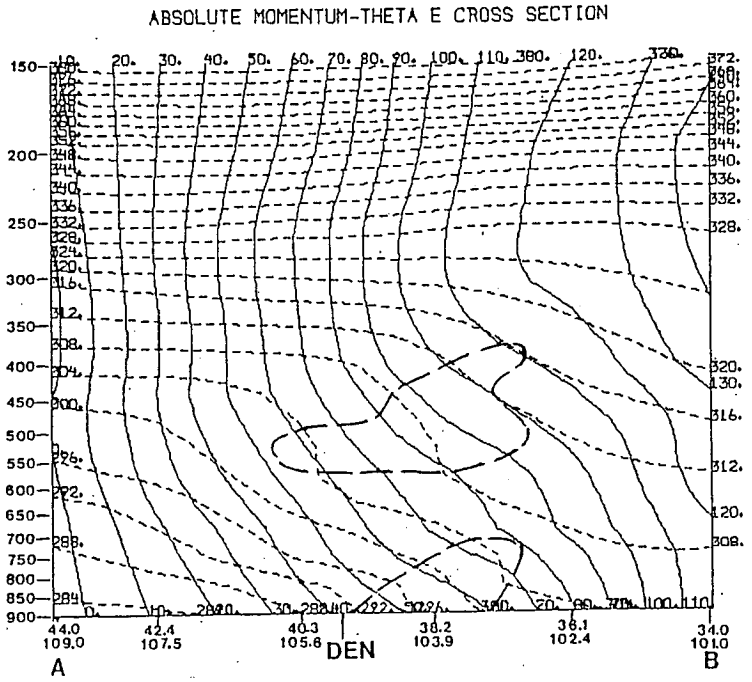

FIG. 6. Vertical cross-section of absolute geostrophic momentum (M_g, solid lines) and equivalent potential temperature (θ_e, dashed lines) for 0000 UTC 20 January 1991. Outlined area denotes region of CSI. Latitude and longitude of points along the cross-section are displayed along the x-axis. (Moore and Lambert 1993)

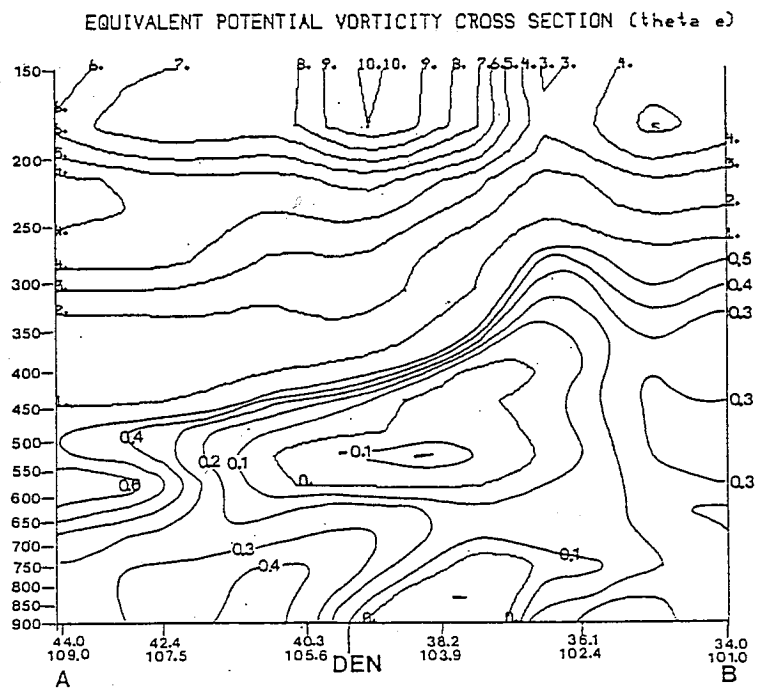

FIG. 7. Vertical cross-section of EPV in PVU (1×10^{-6} m^2 K s^{-1} kg^{-1}) for 0000 UTC 20 January 1991. Negative region depicts CSI. (Moore and Lambert 1993)

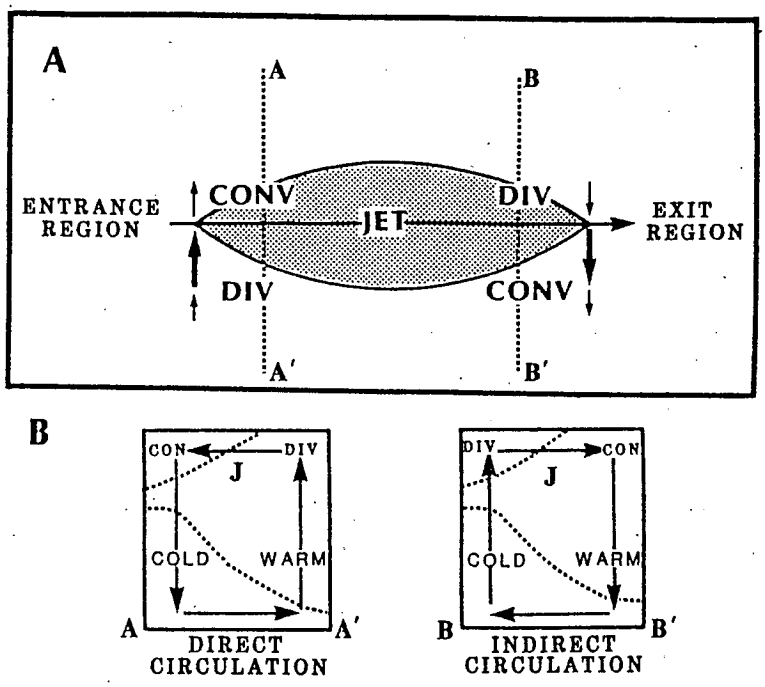

FIG. 8. Schematic of transverse ageostrophic wind components and patterns of divergence associated with the entrance and exit regions of a straight jet streak. (B) Vertical cross-sections illustrating direct and indirect circulations in the entrance region (along dotted line A-A' in A) and exit region (along B-B' in A) of a jet streak. Representative isentropes (dotted) and relative positions of cold and warm air are indicated, as well as horizontal ageostrophic components and vertical motions (arrows) within the plane of each cross-section. Upper-level jet location is indicated by "J" and areas of convergence/divergence labeled. (From Uccellini and Kocin 1987)

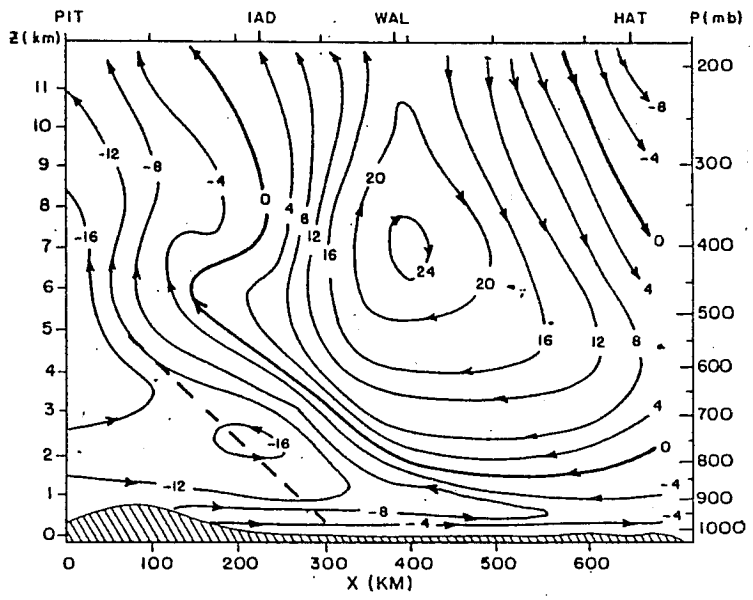

FIG. 9. The ageostrophic mass streamfunction (10^2 m mb s^{-1}) at 1200 GMT 11 February 1983, in a vertical plane from Pittsburgh, PA to Hatteras, NC. Heavy dashed line shows axis of maximum frontogenetical forcing. See Sanders and bosart (1985) for more details. (From Emanuel 1985)

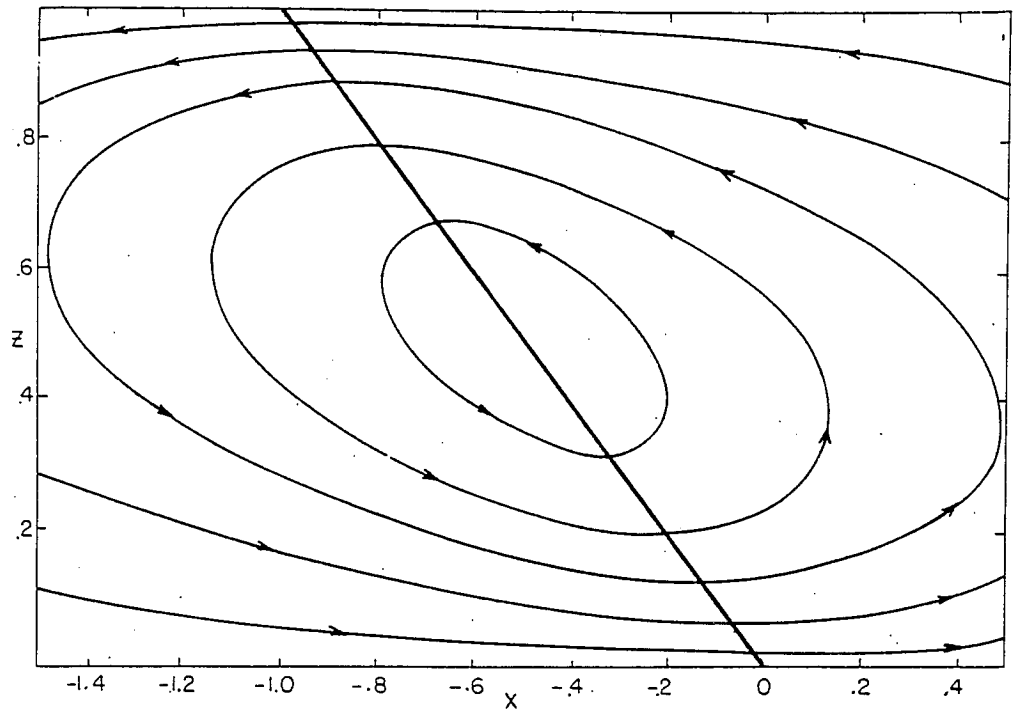

(A)

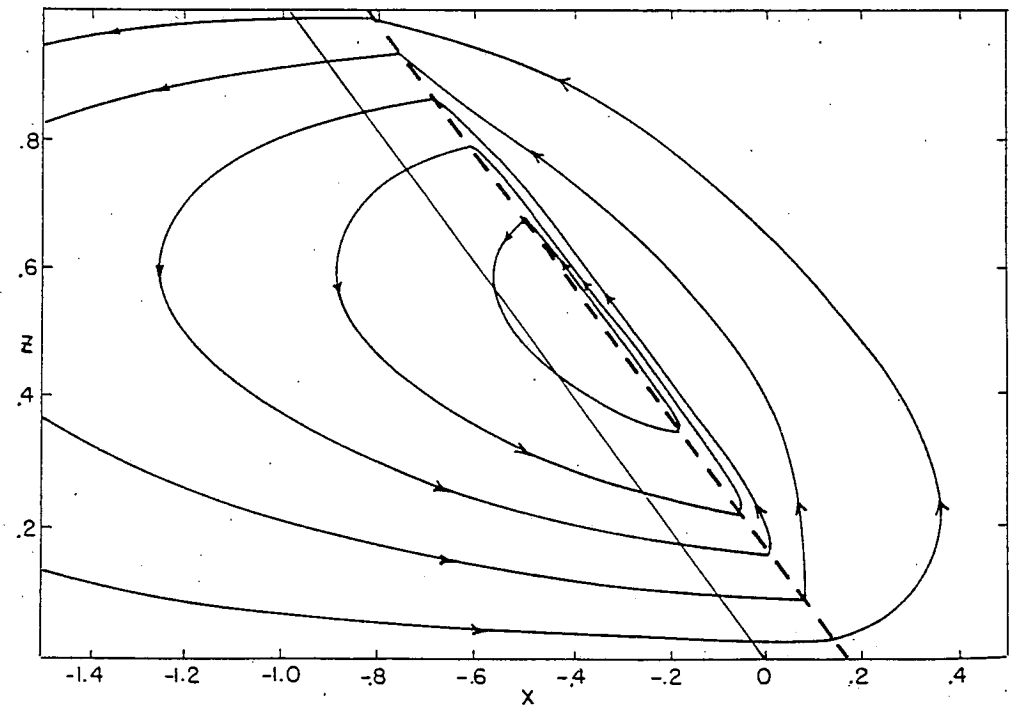

(B)

Fig. 10. (A) Vertical circulation in the vicinity of a front in typical synoptic conditions (where vorticity is cyclonic and large in magnitude - not conducive to CSI circulations). (B) Vertical circulation in the vicinity of a front in the presence of small or neutral symmetric stability. (from Bluestein 1993)

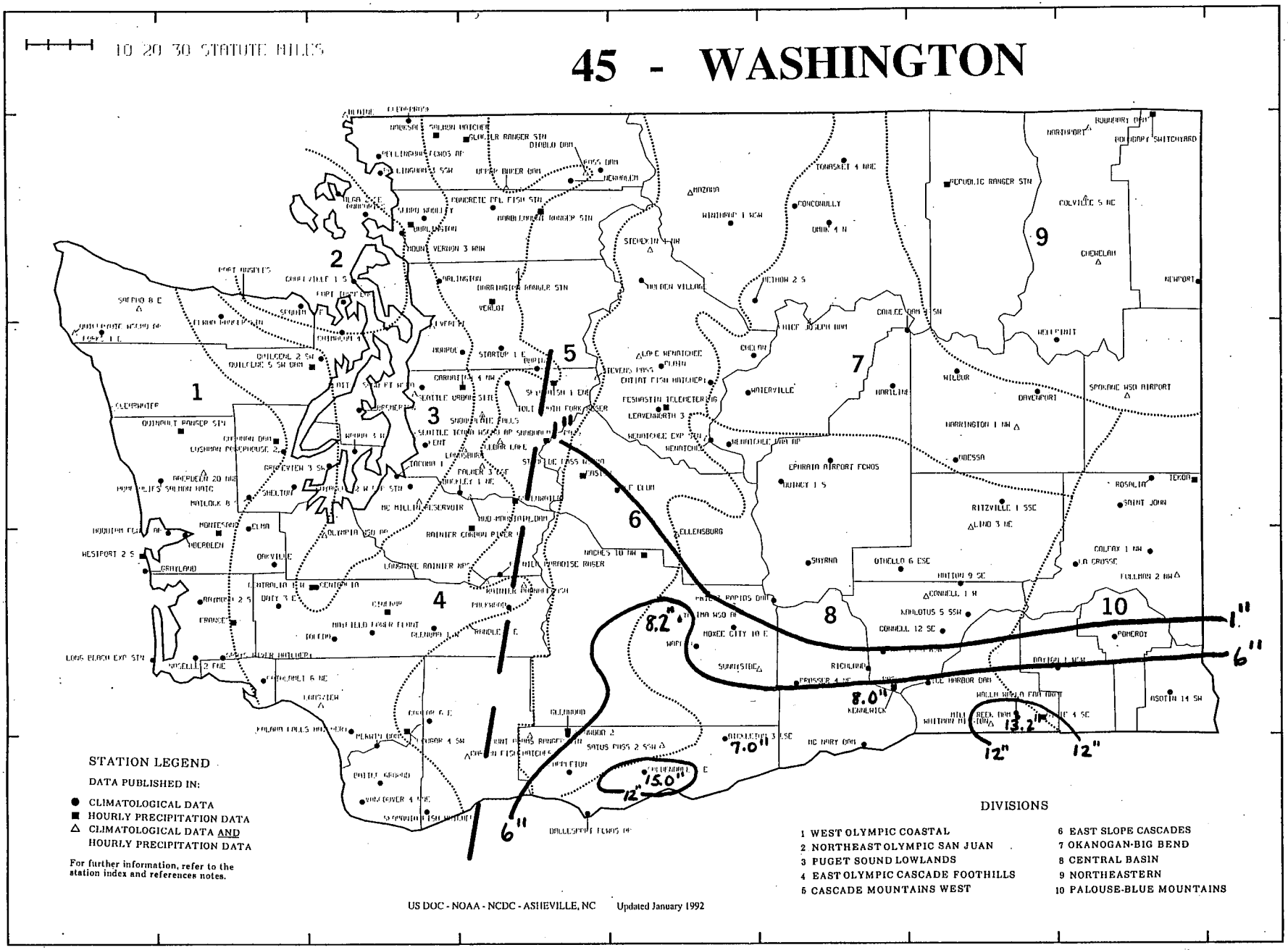

FIG. 11. Snowfall totals (in inches) from the 23-24 February 1994 snowstorm in Washington.

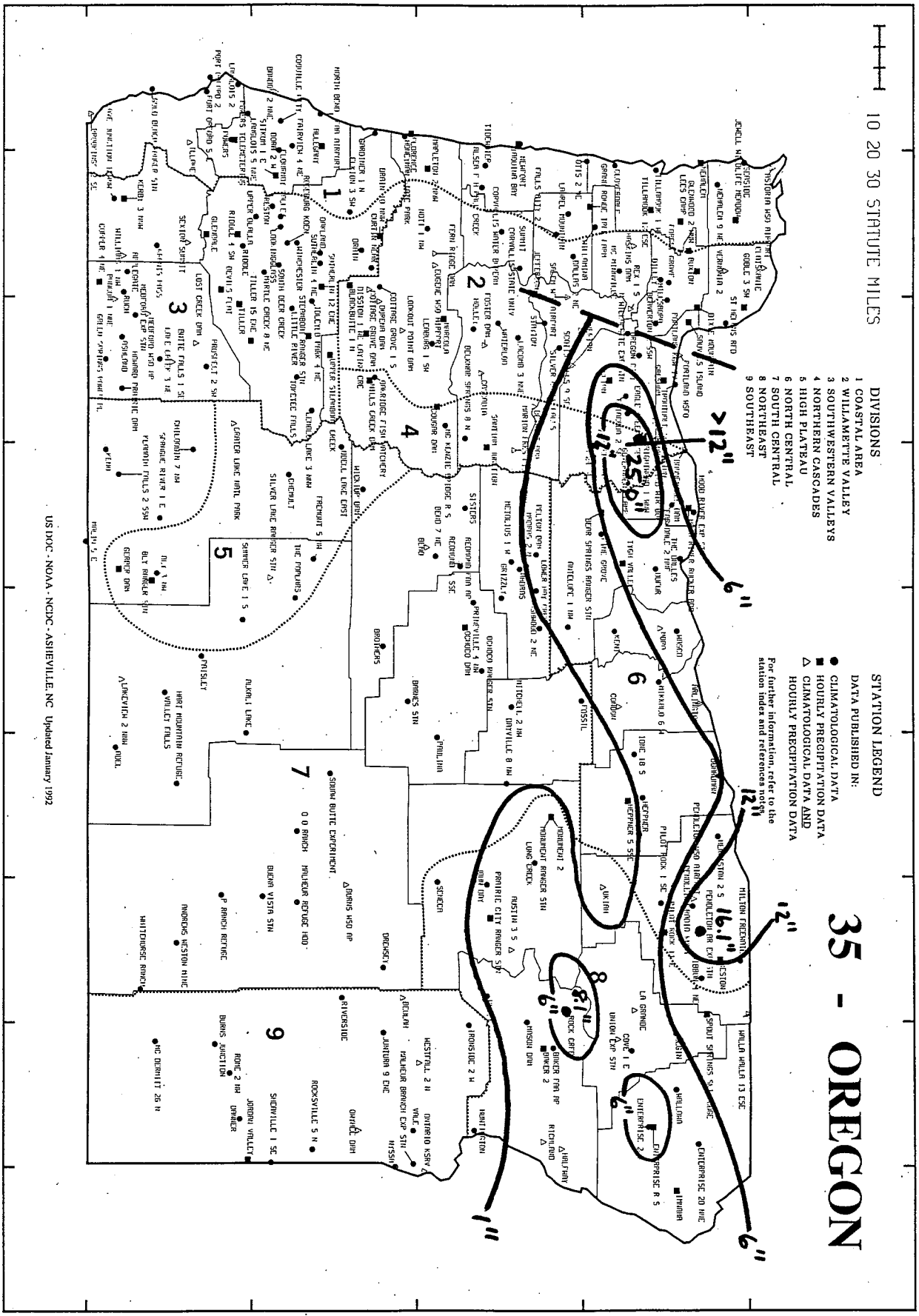

FIG. 12. Snowfall totals (in inches) from the 23-24 February 1994 snowstorm in Oregon.

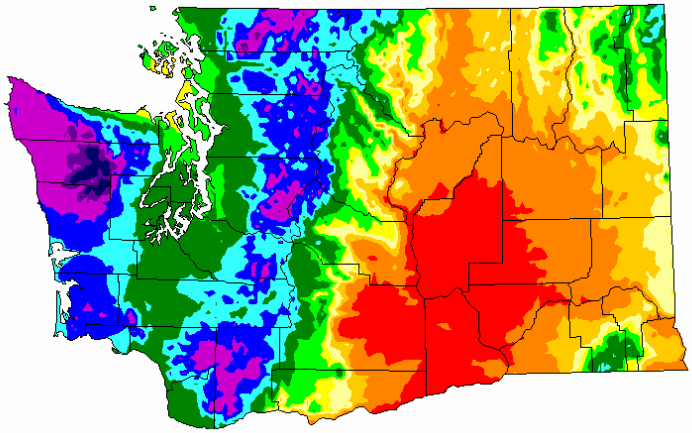

Mean Annual Washington Precipitation 1961-1990
FIG 13

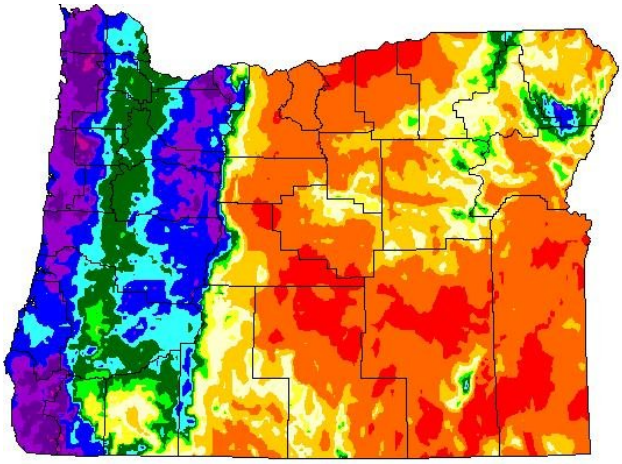

Mean Annual Oregon Precipitation 1961-1990
FIG 14

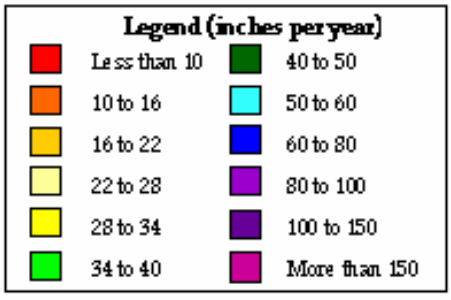

FIGS 13-14. Mean annual precipitation maps for Washington and Oregon. Climatological period: 1961-1990. (Oregon Climate Service)

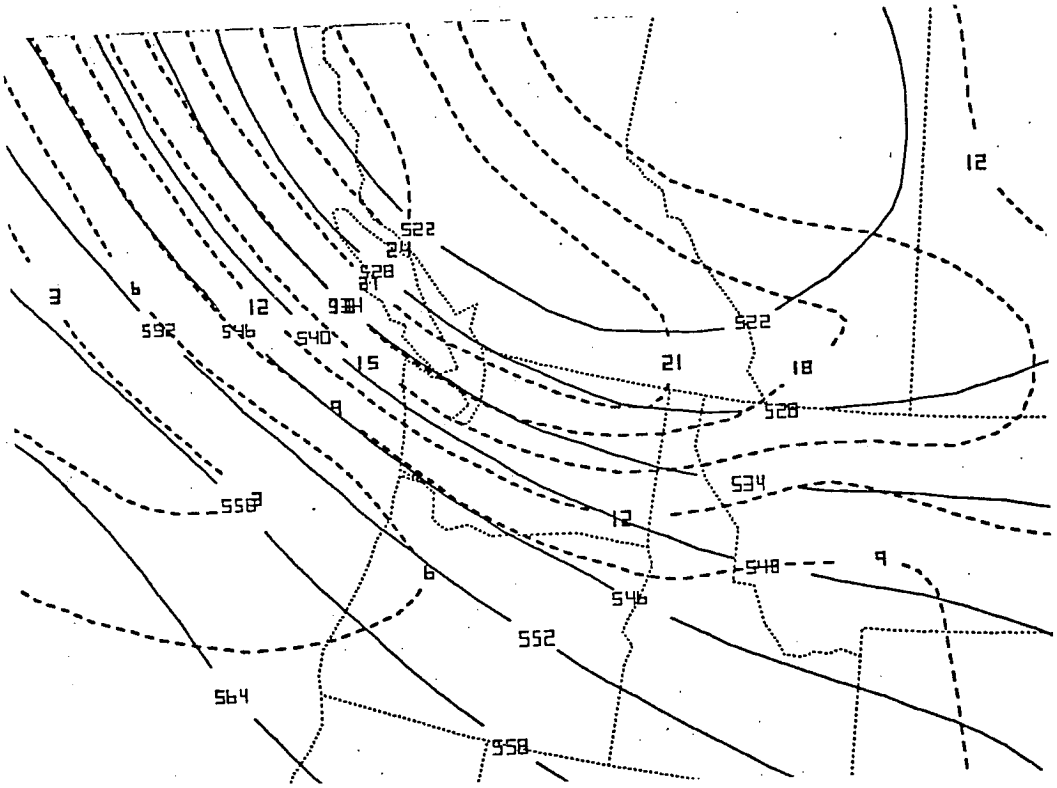

FIG. 15. NGM 00-hour 500 mb geopotential heights (solid lines, every 6 dam) and absolute vorticity (dashed lines, every 2 x 10^{-5} s^{-1}) at 0000 UTC 24 February 1994.

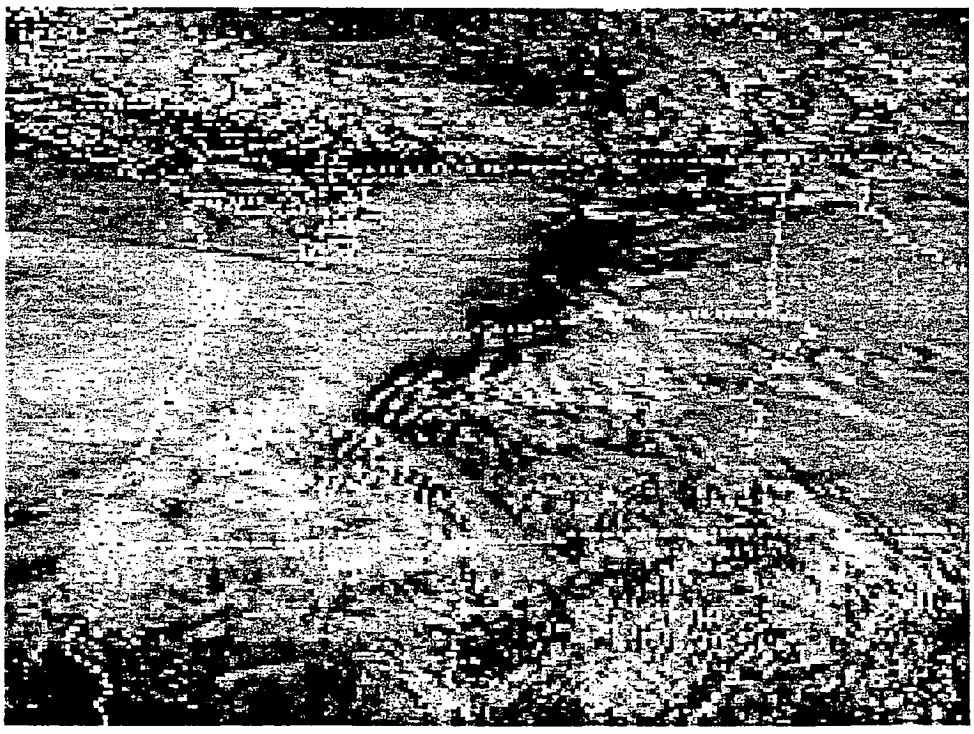

FIG. 16. GOES-7 visible imagery over the Pacific Northwest at 2300 UTC 23 February 1994.

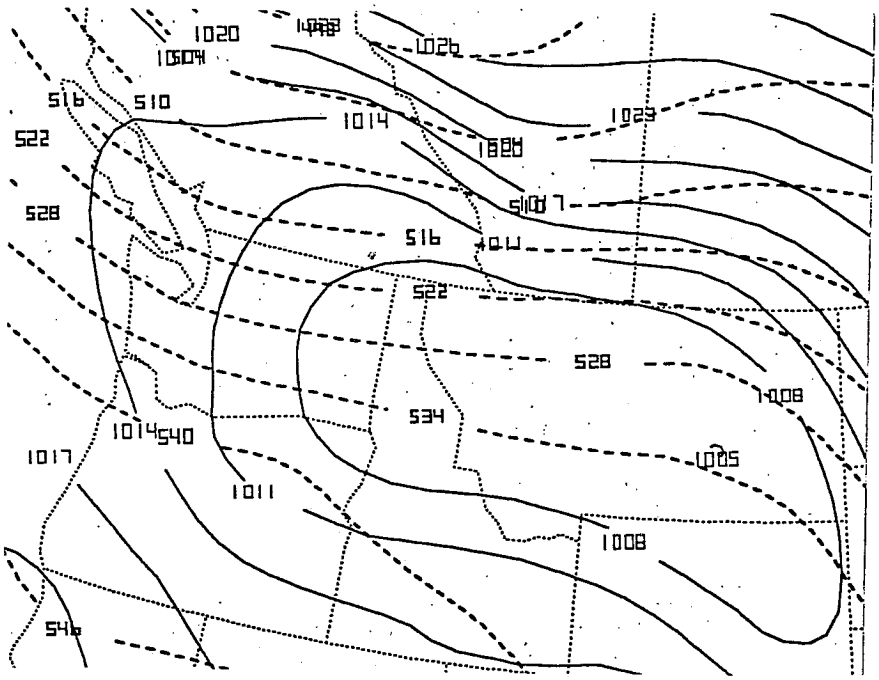

FIG. 17. NGM 0000 UTC 24 February 1994 mean sea level pressure (solid lines, every 3 mb) and 1000-500 mb thickness (dashed lines, every 6 dam) over the Pacific Northwest.

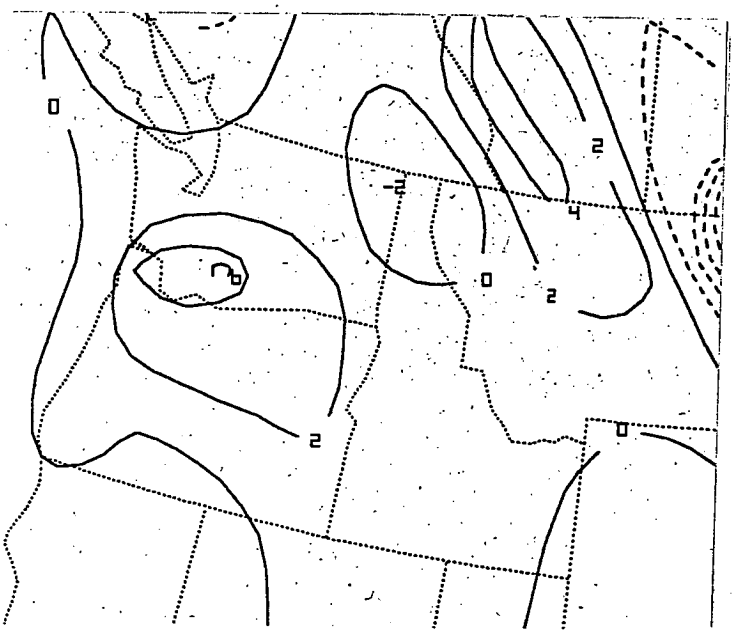

FIG. 18. NGM 0000 UTC 24 February 1994 calculation of 850-mb quasi-geostrophic frontogenesis.

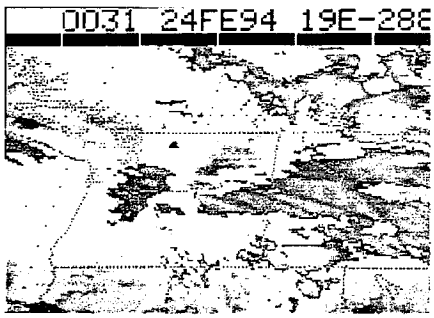

a.

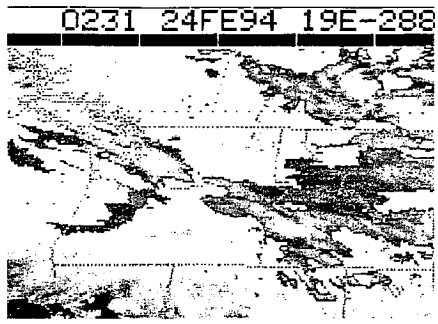

b.

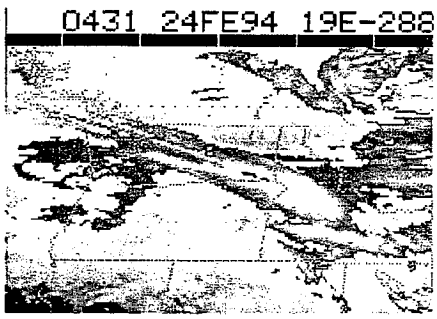

c.

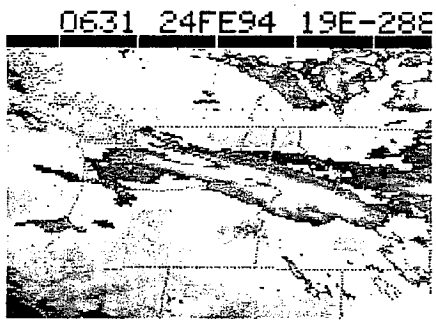

d.

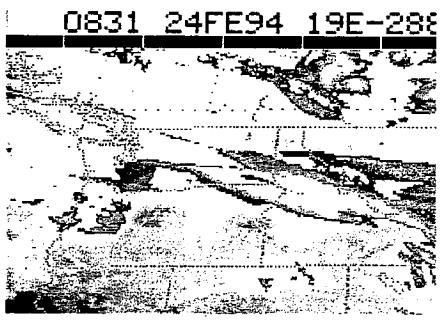

e.

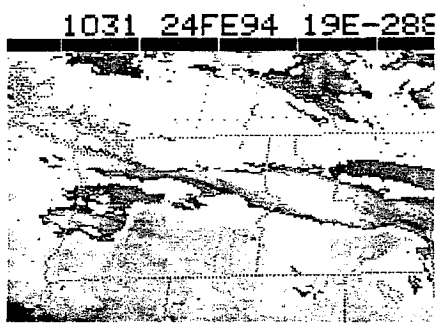

f.

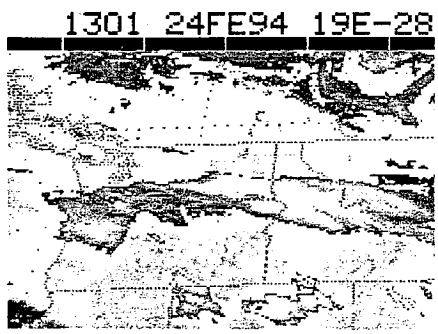

g.

FIG. 19 (a-g). Time sequence of GOES-7 IR imagery over the Pacific Northwest from 0030 UTC 24 February 1994 to 1301 UTC 24 February 1994.

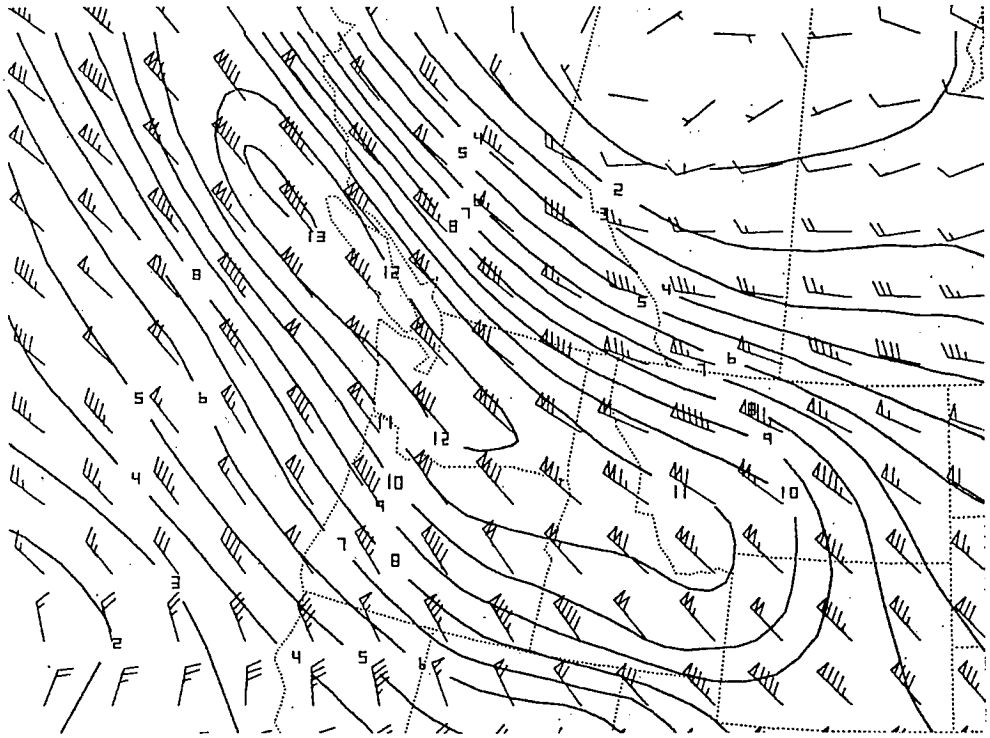

Fig. 20. NGM 00-hour 300-mb isotachs at 0000 UTC 24 February 1994, contoured every 10 kts.

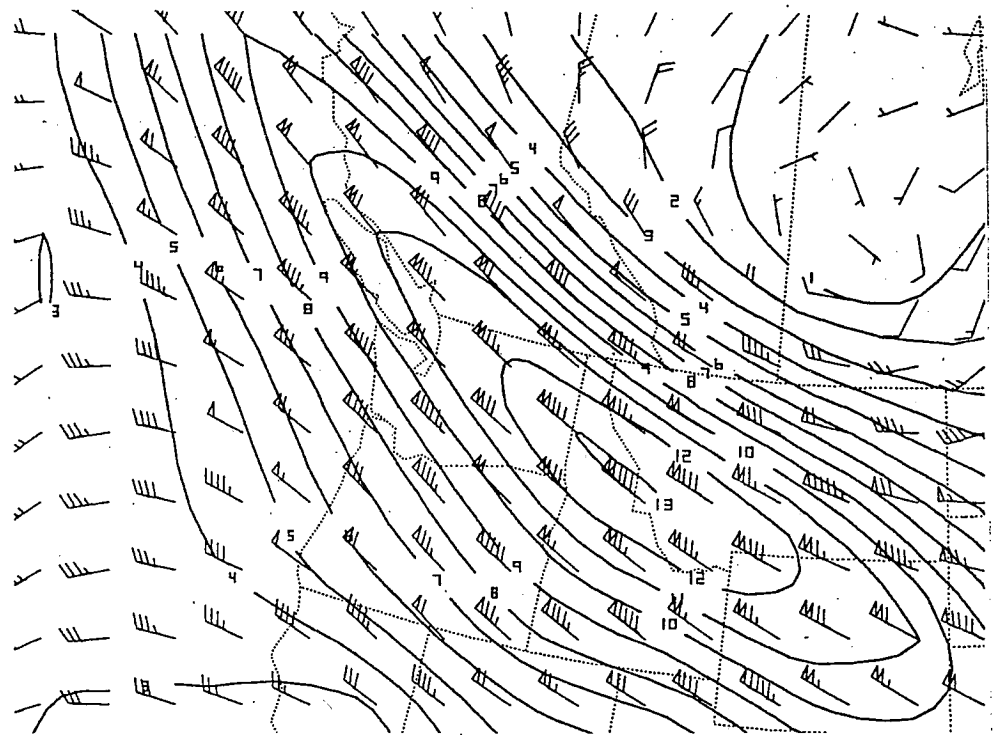

Fig. 21. NGM 12-hour forecast of 300-mb isotachs valid at 1200 UTC 24 February 1994, contoured every 10 kts.

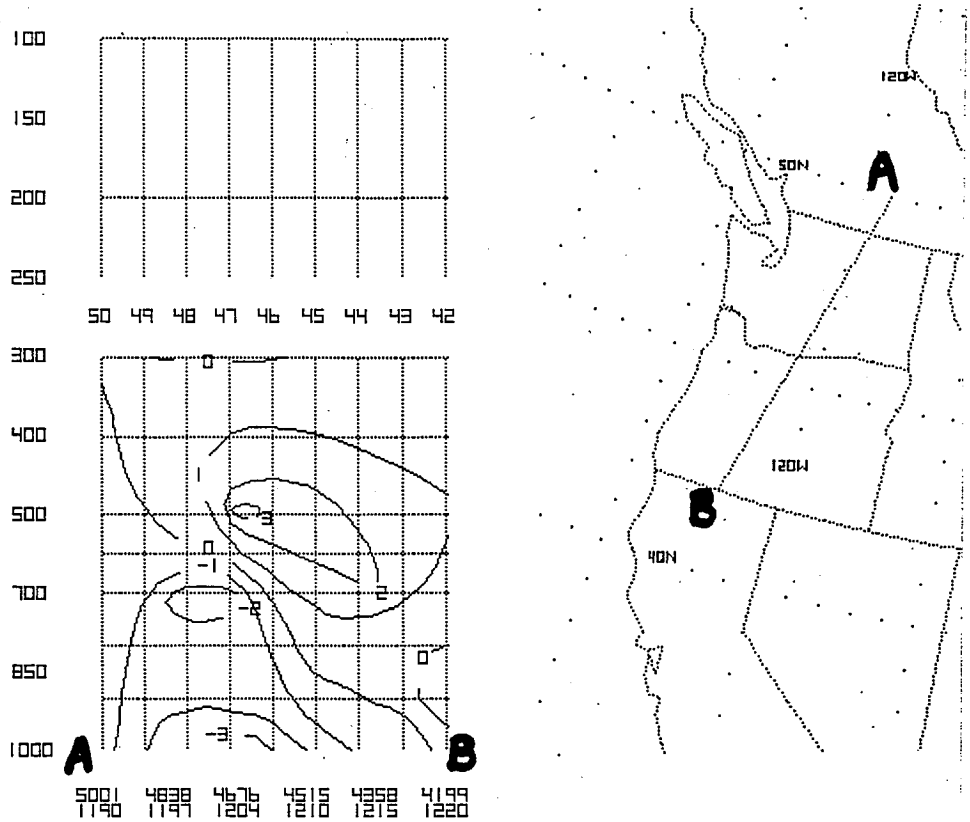

FIG. 22. NGM cross-sectional computation of moisture (mixing ratio) advection by the total wind at 1200 UTC 24 February 1994.

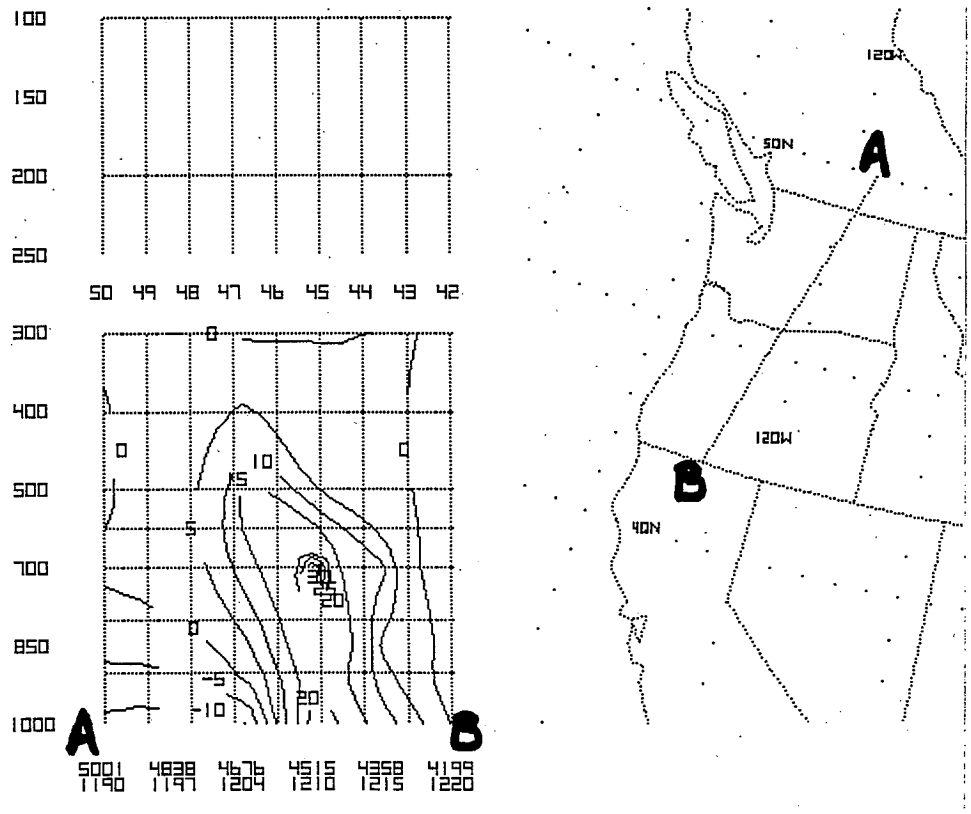

FIG. 23. NGM cross-sectional computation of moisture (mixing ratio) advection by the ageostrophic wind at 1200 UTC 24 February 1994.

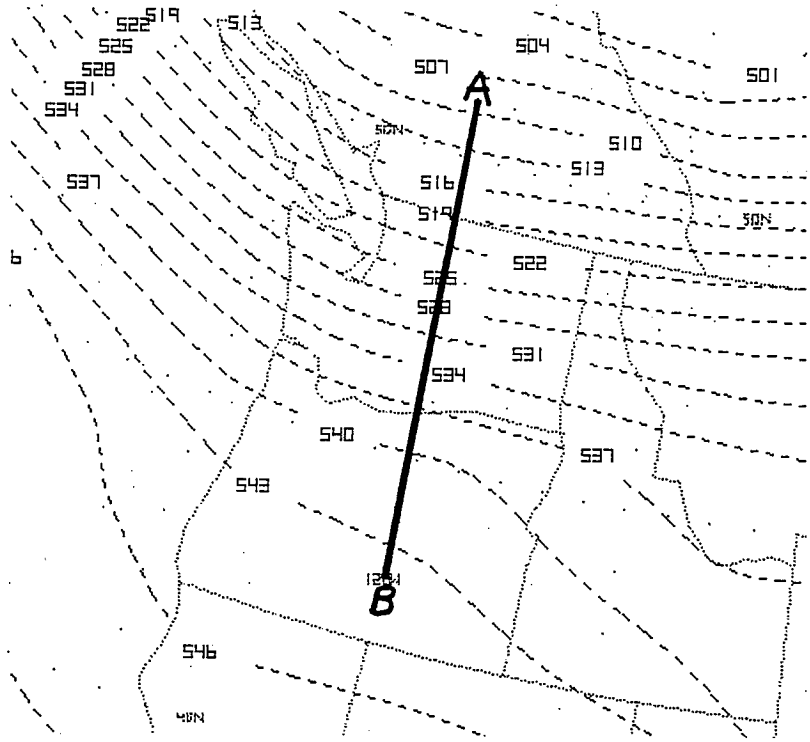

FIG. 24. Path (A to B) of vertical cross-section shown in Fig. 26.

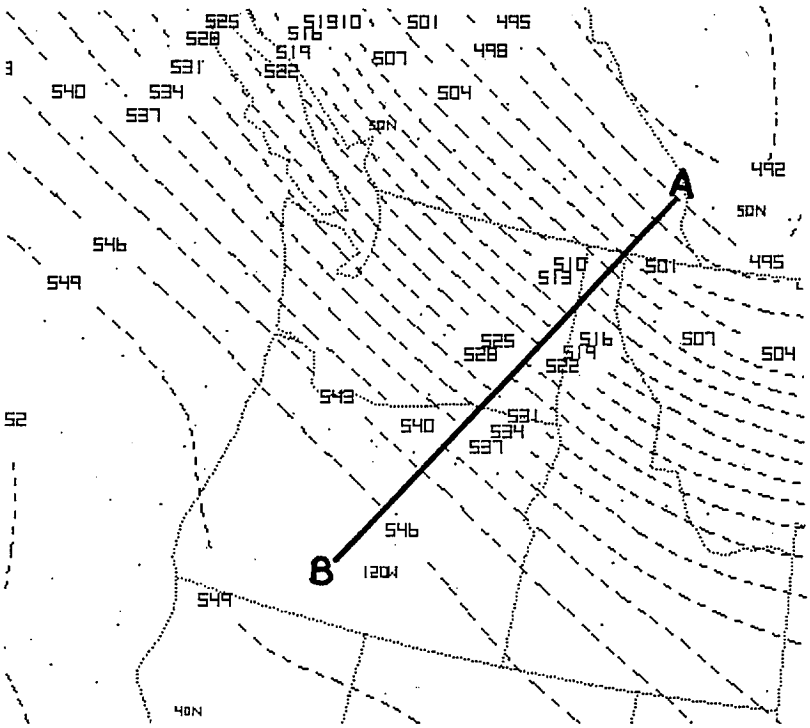

Fig. 25. Same as 24 except path (A to B) for Fig. 27.

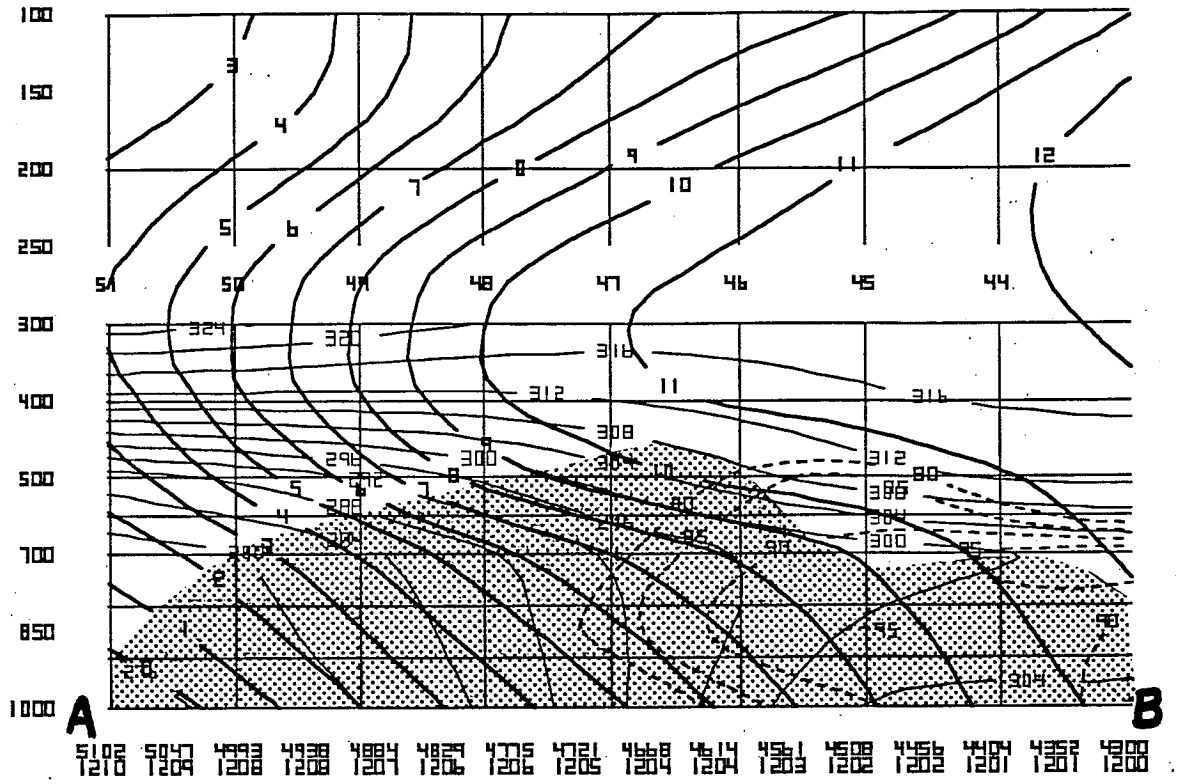

FIG. 26. NGM 0000 UTC 24 February 1994 vertical cross-section of M_g (thick solid lines, at intervals of 10 knots) and θ_e (thin solid lines, at intervals of 4 degrees Kelvin). Relative humidities greater than 80% are dashed at intervals of 5%. Areas where the slopes of M_g surfaces are less than those of θ_e surfaces are shaded. Note the area of convective instability to the south of 46 degrees north latitude.

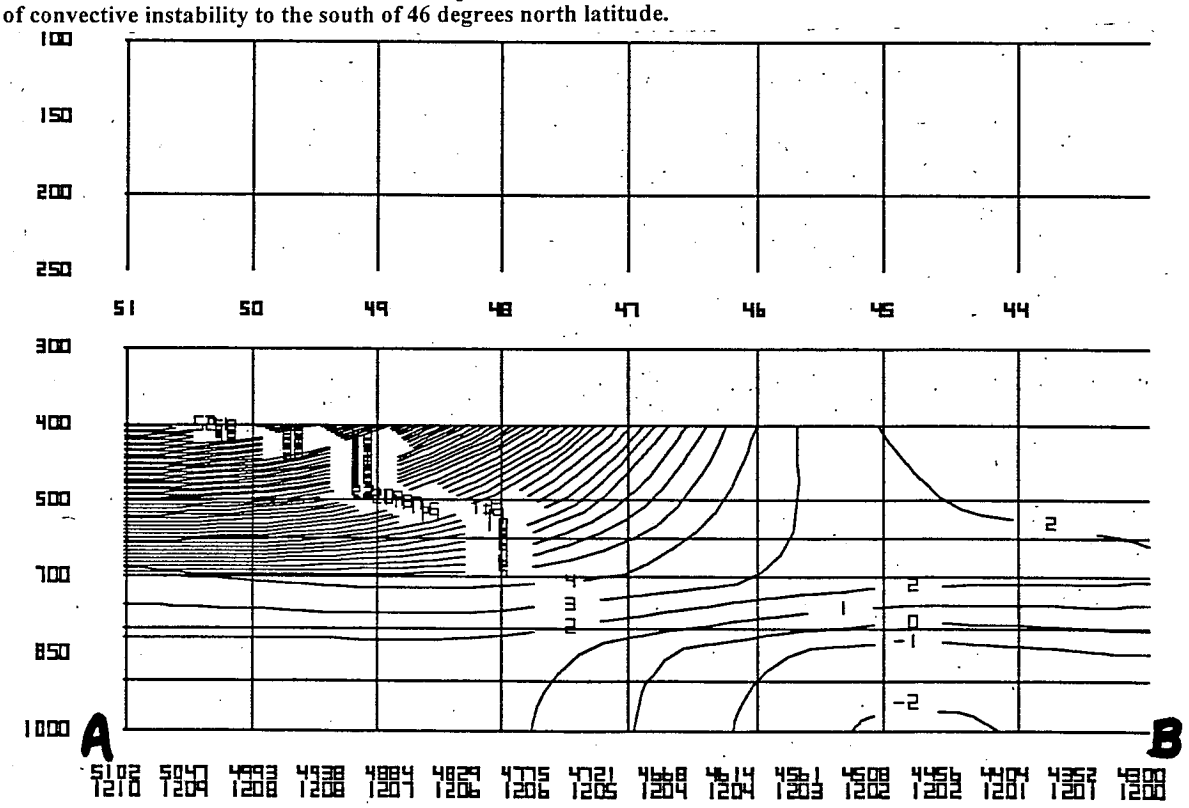

FIG. 27. NGM 0000 UTC 24 February 1994 vertical cross section of equivalent potential vorticity (EPV). Areas of negative EPV denote areas of CSI.

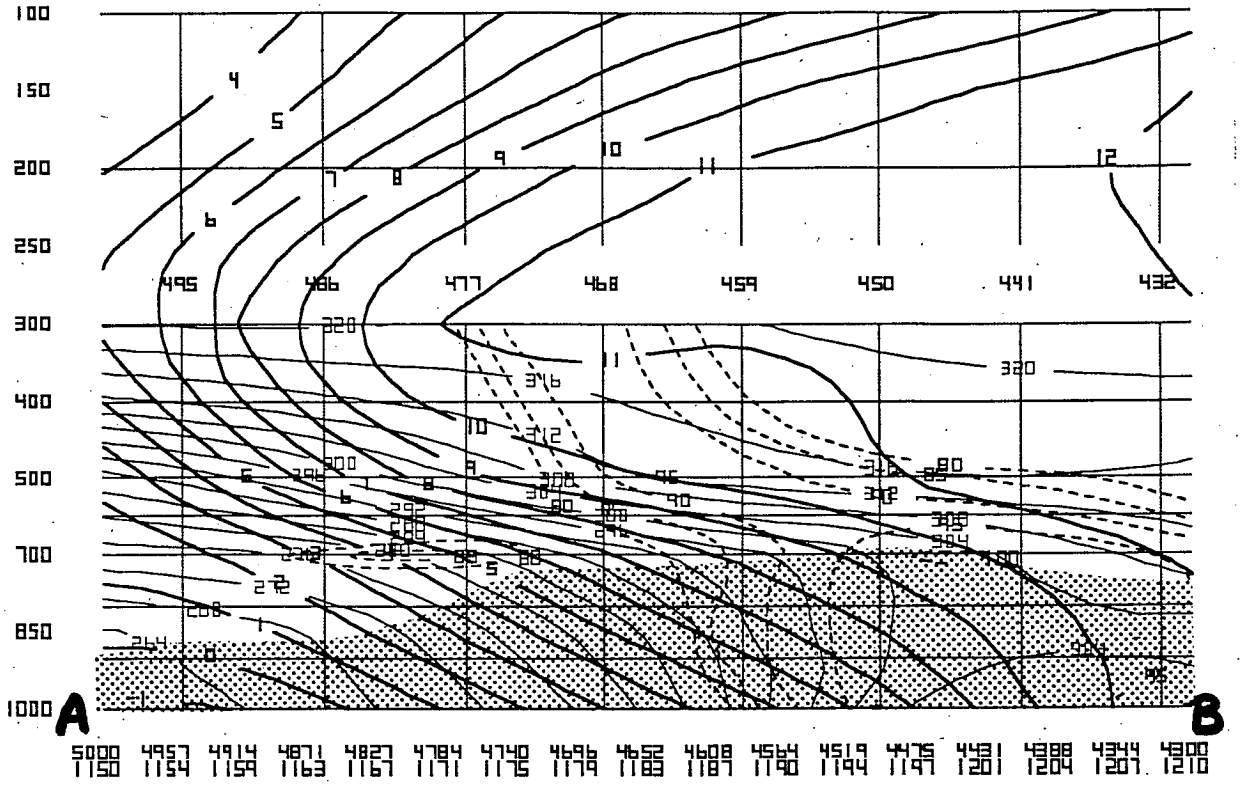

FIG. 28. Same as Fig. 26 except valid at 1200 UTC 24 February 1994.

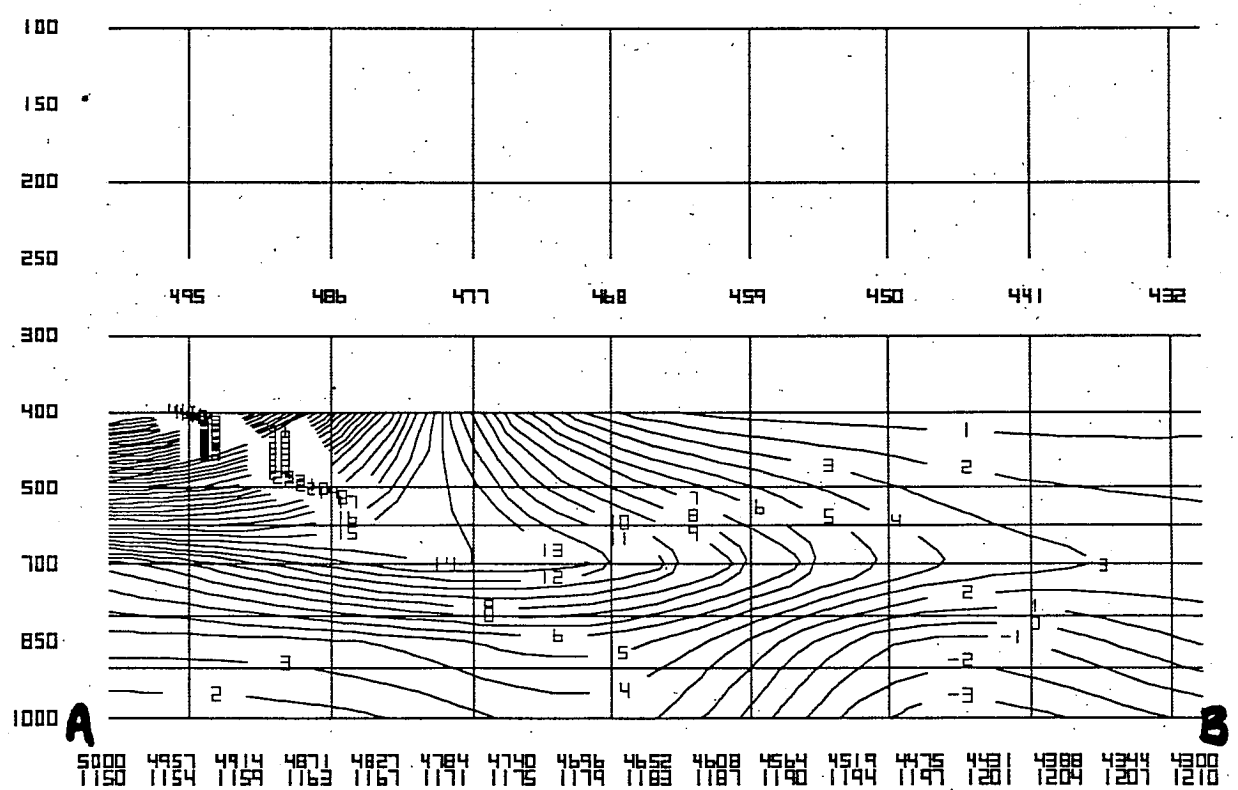

FIG. 29. Same as Fig. 27 except valid at 1200 UTC 24 February 1994.

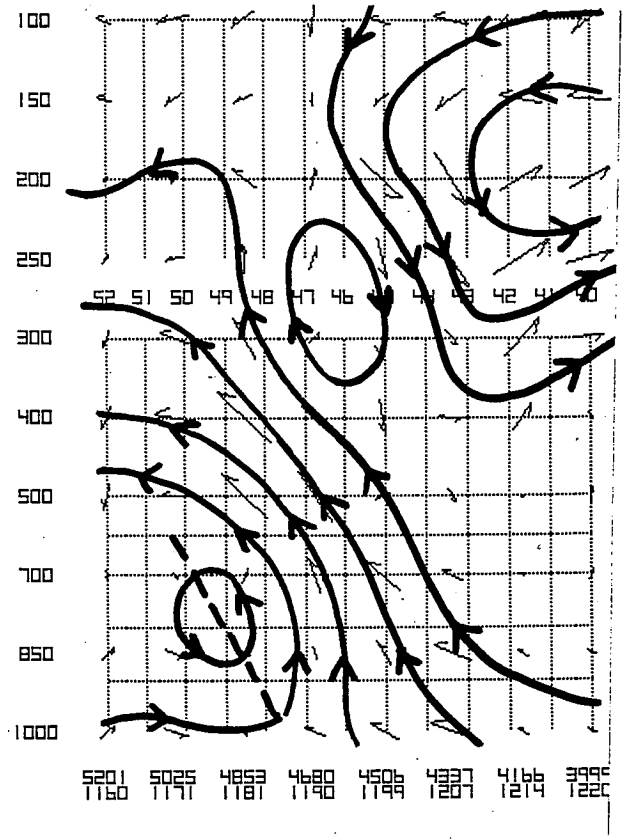

FIG. 30. NGM 00-hour ageostrophic circulation (solid black arrows) valid at 1200 UTC 24 February 1994. Estimated ageostrophic mass streamfunction (solid black lines) is overlaid. Solid dashed line marks area of maximum frontogenetical forcing.

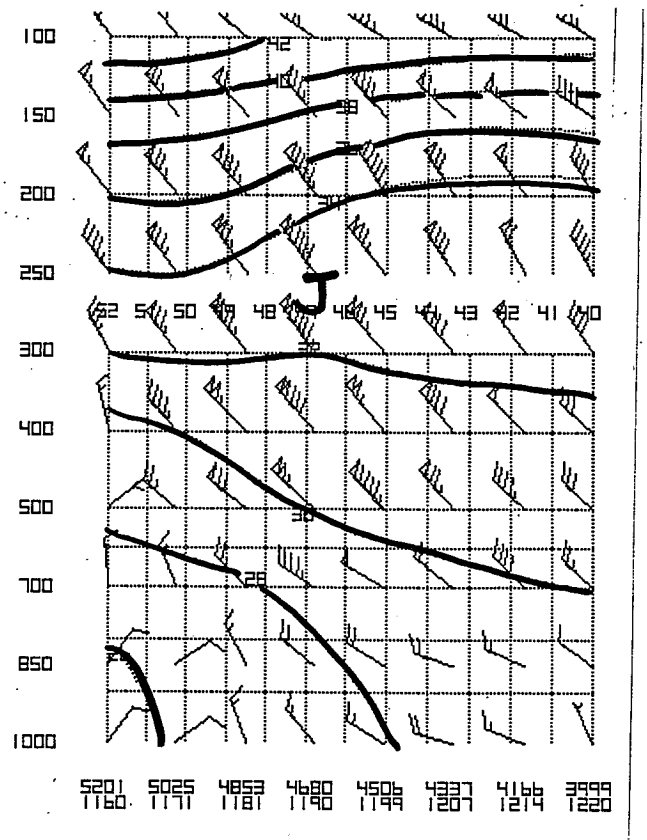

FIG. 31. NGM 00-hour plot of wind barbs (knots) and potential temperature (solid lines, every 2 degrees Kelvin) valid at 1200 UTC 24 February 1994. "J" marks position of upper level jet.